Georgios Pouliasis

Investigating the dependencies of individual overtopping volumes on vertical wall breakwaters under non-breaking waves

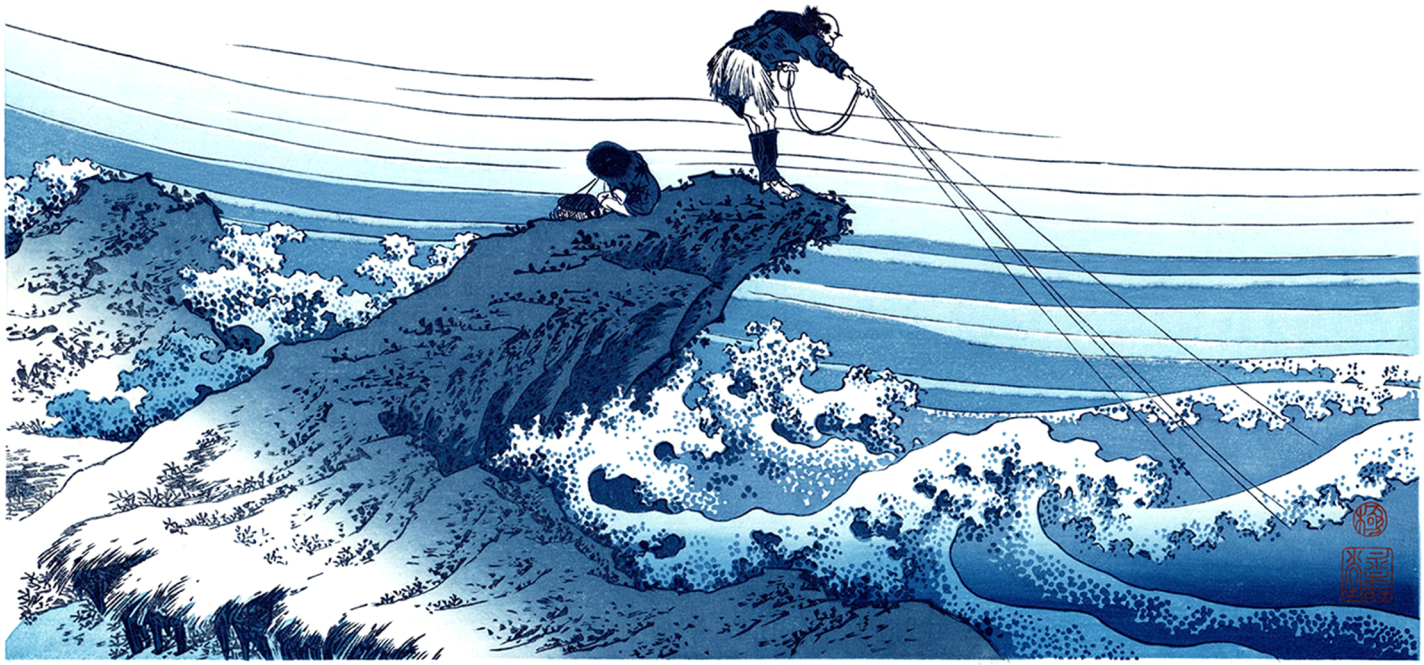

TU Delft

Investigating the dependencies of individual overtopping volumes on vertical wall breakwaters under non-breaking waves

by

Georgios Pouliasis

to obtain the degree of Master of Science
at the Delft University of Technology,
to be defended publicly on Tuesday September 19, 2023 at 10:45 AM.

Student number: 4805704
Project duration: November 30, 2020 – September 19, 2023
Thesis committee:

Dr. ir. A. Antonini,	TU Delft, supervisor
Dr. ir. B. Hofland,	TU Delft
Dr. ir. O. Morales-Napoles,	TU Delft
Prof. Dr. ir. M.R.A. van Gent,	TU Delft, Deltares

An electronic version of this thesis is available at http://repository.tudelft.nl/.

Cover design: Antonio Paoletti
Original painting: Katsushika Hokusai, A Fisherman Standing on a Rocky Promontory at Kajikazawa in Kai Province

TU Delft

Preface

The completion of this thesis marks the end of my studies at TU Delft. This journey has lasted 5 years, 3 years more than the nominal duration of the program. A journey that started under different circumstances than the present, from a different person than the one who is writing these lines. It suffices to say that during this time I struggled very hard. But, as I reflect on this journey, I firmly believe that today finds me in a better place than the one I was yesterday.

Contemplating back on this time, I cannot help but feel gratitude for the people who supported me and of-course for the people who have contributed in this thesis. Firstly, I would like to thank Alessandro Antonini and Oswaldo Morales-Napoles for believing in me at a time where I had little motivation myself. Moreover, I would like to thank them and the other members of my committee, Bas Hofland and Marcel van Gent for their great insight, keen observations, mentorship but also understanding and patience during the long duration of this thesis. Also, I would like to express my gratitude to Aggelos Dimakopoulos and Graham Siggers for our fruitful conversations and for reviewing this document. Moreover, I would like to thank Robert Lanzafame for the collaboration and advice.

On a personal level, I would like to express my gratitude to my friends Antonio, Lucija, Amina, Dimitris D., Dimitris B., Alexandra and Petros for their commitment, support and for the fun we had. Our time together is something that I will cherish for long. Naturally, I could not forget to mention my parents, Aimilios and Maria. Thank you for your love and selfless struggle. Thank you for laying the foundation for me to follow my path. Last but not least, I would like to thank Maria, my partner, who has stood beside me for all of these years. Your smile makes me smile. To her I dedicate this work.

G. Pouliasis
Reading, September 2023

This city, which used to be full of love and courage, these years was full only with courage, because her love became an act of courage.
...
Η πόλη αυτή, η γεμάτη έρωτα και παλληκαριά, τούτα τα χρόνια ήταν γεμάτη μόνο παλληκαριά, γιατί και ο έρωτας της έγινε παλληκαριά.
Μενέλαος Λουντέμης, Οδός Αβύσσου Αριθμός 0

Contents

Abstract

Wave overtopping of coastal structures is generally expressed in terms of average discharge and maximum overtopping volume. While substantial research can be found on the relationship of such variables with incident spectral characteristics and other geometrical dimensions, limited research has been done to identify the conditions for which severe individual overtopping events occur. The objective of the present work is to further investigate the statistical dependencies between individual overtopping volumes and incident wave characteristics and to identify the conditions which result in maximum overtopping events. To this aim, we statistically analyse timeseries of waves and overtopping events for the case of a vertical wall breakwater on a horizontal bed under non-breaking wave conditions. The timeseries are generated using a validated numerical model for 6 sets of boundary conditions. The analysis of the data shows that, among the examined variables, the incident wave crest level at the toe of the structure has the highest rank correlation with the individual overtopping volumes. Conversely, the incident wave heights show a lower rank correlation while the wave periods show no correlation at all. Additionally, by leveraging the tool of copulas we find that the incident wave crest levels have strong upper tail dependence with the individual overtopping volumes while the wave heights show no tail dependence. Subsequently, we examine possible dependencies with the wave group periods and wave group energy. We find that a moderate correlation exists between wave group periods and overtopping volumes but no upper tail dependence. Moreover, our results show that the fraction between the wave group energy and the group period has a high correlation and upper tail dependence with the overtopping volumes. Finally, we discuss possible practical applications of our findings as well as points for future research.

1

Introduction

Overtopping is one of the key parameters in the design of breakwaters. The overtopping volume severity influences structural aspects, such as stability and crest elevation, operation, damage to property, as well as access to the public. Traditionally, overtopping is expressed in terms of the average overtopping discharge q. However, average quantities provide only minimal information of the actual distribution of the overtopping events. For example, a structure which overtops frequently with low volumes and a structure which rarely overtops with large volumes may have the same average discharge, however the extreme response of the latter may be more severe. The importance of the maximum overtopping volume V_{max} was acknowledged early on in the work from Franco et al. (1995), however the guidance provided at the time only included permissible mean overtopping discharges. Later on, the overtopping manual (*EurOtop (2007)*) (Pullen et al., 2007) provided guidelines related to maximum individual overtopping volumes which where further improved in the later version of 2018 (van der Meer et al., 2018). The aforementioned manuals provide relationships to estimate V_{max} which are based on the Weibull distribution. The parameters are associated with incident wave characteristics, such as the significant wave height H_s and peak period T_p, the geometrical features (i.e. freeboard R_c and structure slope) and local bathymetry. More recently, other researchers have expanded the formulations reflect different structures and wave conditions. For example Mares-Nasarre et al. (2020) and Molines et al. (2019) examined the effect of breaking waves and a shallow foreshore on the distribution parameters. For a thorough review of the recent advances the reader is referred to the work by Koosheh et al. (2021).

Despite the considerable research on the distribution of overtopping volumes, little research has been done to correlate the wave characteristics to the individual overtopping volumes, e.g. the incident wave height with the corresponding overtopping volume. Gunbak and Bruun (1979) provided a discussion on the effect of sequences of waves in the stability and overtopping of rubble mound breakwaters based on small scale physical experiments. They suggested that a modest amplitude wave of a particular period succeeded by a larger wave of shorter period will produce high overtopping. According to their observations, the shorter period wave can propagate on the crest of the preceding longer wave, effectively generating large amounts of overtopping. More recently, Hofland et al. (2014) performed long duration tests of 10000 irregular waves and measured overtopping over a smooth sloped dike with a slope of 1/3. They found that there was not a specific wave height threshold above which waves overtopped. Moreover, their evidence suggests that there is not a one to one relation between the incident wave height and overtopping volume. This implies that the largest incident wave height will not necessarily result in the largest overtopping volume. Additionally, they found that the largest correlation between wave characteristics and overtopping events occurred about one wave period prior to the event. Whittaker et al. (2018) conducted physical and numerical experiments to investigate the overtopping volumes of focused wave groups, using the NewWave theory (Tromans et al., 1991), over an inclined wall. They found that for a given linear amplitude and focus location, changing the wave phase can lead to an order of magnitude difference in the total overtopping volume of the wave group. All of the above provide evidence that the wave height may not necessarily be the best predictor of maximum overtopping volumes. Moreover, there may exist a certain combination of wave heights and periods, which could be described by a wave group, that constitutes critical conditions for severe individual wave overtopping volumes.

In the present work we aim to investigate the statistical relations between individual overtopping volumes and incident wave characteristics in order to further the understanding of the contributing factors to severe overtopping volumes. Since, to the authors' knowledge, this is a novel attempt, we focus our investigation on the simplest case possible, a vertical wall breakwater on a horizontal bed under the influence of non-breaking waves. The statistical analysis is conducted on a data set of simulated overtopping volumes using OpenFOAM. Our numerical model is validated against experimental data generated at the wave flume of Hydraulic Engineering Laboratory, Delft University of Technology. During the numerical simulations we vary the boundary conditions to test the effect of different parameters, namely the significant wave height, the peak period and the spectral shape (JONSWAP and Pierson-Moskowitz). As a first step the correlation between incident wave variables and overtopping volumes is examined using a simple rank correlation metric. Subsequently, the critical variables are identified and the dependence structure with the individual overtopping volumes is investigated using copulas. Copulas are joint distributions with uniform marginals and have the advantage to describe the dependence structure separately from the marginal distributions. In the fields of marine and coastal engineering they have been used for, among other applications, the construction of synthetic timeseries of metocean conditions (e.g. (Corbella & Stretch, 2013; De Michele et al., 2007; Jäger & Nápoles, 2017; F. Li et al., 2014)) and the derivation of extreme design conditions (Lanzafame et al., 2021; Orcel et al., 2021). Additionally, copulas have been used by Dong et al. (2015) to study the joint distribution between wave group heights and group periods and by Zhang et al. (2018) to examine the relationship between wave height, wave period and wind velocity. In the present paper, copulas are utilised to derive information about the joint tails of the individual overtopping volumes and the identified critical variables for overtopping. Subsequently, after the statistical analysis of incident individual waves, we examine the contribution of incident wave groups to the overtopping volumes by examining their dependence using rank correlations and copulas.

The structure of the present paper is as follows. Firstly a brief introduction about the numerical tools employed herein is provided, followed by the numerical model validation. Next, some remarks about the interface capturing method employed are presented. Subsequently, the numerical data sets are compared with the empirical relationships from the EurOtop manual. Then we discuss the dependencies between individual overtopping volumes and different incident wave parameters (i.e. wave height, wave period and length,crest and trough level and wave steepness) and explore potential relationships of the overtopping volumes with the incident wave groups. To conclude we provide a summary of our findings and discuss possible practical applications of our work and possibilities for future research.

2

Tools and methods

The numerical simulations herein were performed using the OpenFOAM (Weller et al., 1998) framework and the package waves2foam, developed by Jacobsen et al. (2012). OpenFOAM offers a variety of solvers aimed at different application based on the finite volume discretization of the governing equations. In the current study we are using the Raynolds Averaged Navier-Stokes (RANS) equations to model the wave-structure interaction processes. OpenFOAM has been extensively used to simulate wave-structure interaction(L. Huang et al., 2022) and especially overtopping in a variety of coastal structures, such as vertical wall breakwaters, rubble mound breakwaters (Higuera et al., 2014; Jacobsen et al., 2018; Jensen et al., 2014), dikes (Chen et al., 2021) as well as model complex swash zone processes such as turbulence in breaking waves (Devolder et al., 2018; Y. Li et al., 2020; Patil, 2019).

Waves2foam, is an extension library which provides wave generation and absorption capabilities for some of the existing RANS - VOF solvers. Moreover, it includes a coupling of OpenFOAM with OceanWave3D, which is a fully non-linear potential flow (FNPF) solver (Engsig-Karup et al., 2009). This coupling allows for the wave generation and propagation to be simulated by the more computationally efficient FNPF solver while the wave-structure interaction is simulated by OpenFOAM. This technique constrains the OpenFOAM computational domain in the vicinity of the structure, thus, it effectively reduces simulation times. Furthermore, OcenWave3D includes a flux boundary condition which can be used to input the wave paddle velocity of an actual experiment. This feature enables the validation of the model with experimental data. For the present study the waves2foam library with OceanWave3D were used.

2.1. OpenFOAM

2.1.1. Governing Equations

OpenFOAM is capable of solving the full Reynolds Averaged Navier-Stokes (RANS) equations. To simulate free surface flows, OpenFOAM follows the Volume of Fluid (VOF) method which models the free-surface as the interface of a two-phase flow consisting of water and air. VOF uses an indicator function α to track the different phases. α is a scalar field and it takes the values of 1, when a cell contains only water, and zero, when a cell contains only air. In the interface between the two fluids it takes values between 0 and 1. From that perspective, α can also be seen as a volume fraction, which indicates the water content of a cell. In this manner, fluid properties can be expressed as a function of the volume fraction. The momentum equation, including the Volume of Fluid scalar field α, is given by equation 2.1 (Rusche, 2003):

$$\frac{\partial \rho \mathbf{u}}{\partial t} + \nabla \cdot [\rho \mathbf{u}\mathbf{u}^T] = -\nabla p^* - \mathbf{g} \cdot \mathbf{x} \nabla \rho + \nabla \cdot [\mu \nabla \mathbf{u} + \rho \tau] + \sigma_T \kappa_\alpha \nabla \alpha \tag{2.1}$$

The continuity equation for incompressible fluids is given by equation 2.2:

$$\nabla \cdot \mathbf{u} = 0 \tag{2.2}$$

where:

- ρ: is the fluid density
- $\mathbf{u}$: is the velocity vector (u, v, w)
- p^*: is the excess pressure, i.e. $p^* = p - \rho g h$
- p: is the total pressure
- $\mathbf{g}$: is the gravitational acceleration vector
- $\mathbf{x}$: is the location coordinate vector (x, y, z)
- μ: is the molecular viscosity
- τ: is the Reynolds Stress tensor
- σ_T: is the surface tension coefficient
- κ_α: is the surface curvature
- α: is a scalar field used to denote the fluid phase

For the purposes of the present study, only cases with limited or no breaking were examined, therefore, turbulence was not included in the model. Thus, the Reynolds Stress tensor term from equation 2.1 can be neglected. The surface tension coefficient for fresh water is generally assumed to equal $0.07 kg/s^2$ (Jacobsen et al., 2012) and this value was used in the present study.

2.1.2. VOF solvers

Currently, two VOF solvers are supported in OpenFOAM and waves2foam, interFoam and interIsoFoam. Each of them uses a different algorithm to capture the interface between fluids. interFoam models the evolution of the scalar field using an advection equation with an added artificial compression term to ensure a sharp interface. This equation is solved using MULES (multidimensional universal limiter for explicit solution) (Rusche, 2002). interFoam has seen extensive use in coastal engineering applications (Brown et al., 2016; Castellino et al., 2018; Higuera et al., 2013; Martins et al., 2017; Raby et al., 2020). Despite it's popularity, a comprehensive study by Larsen et al. (2019) showed that interFoam produces wiggles along the interface, spurious air velocities and smearing of the interface along many cells. According to their work it is possible to obtain good results by specifying the simulation time step according to a Courant–Friedrichs–Lewy (CFL) condition in the order of 0.05.

In contrary to the previous method, interIsoFoam utilises the isoAdvector method which handles the interface advection problem by explicitly reconstructing the interface, which is then advected in a geometric manner. For further information on the method the reader can refer to the work from Roenby et al. (2016, 2019). This approach mitigates the smearing and the wiggles of the interface, thus providing improved accuracy in the propagation of waves (Larsen et al., 2019; Patil, 2019; Roenby et al., 2017), the simulation of wave-structure interaction (Chen et al., 2021; van Gorsel, 2021) and recently, flows through porous media (Missios et al., 2023). For those reasons, in the present study, we chose to employ interIsoFoam and isoAdvector for the simulation of the numerical experiments. Despite this, we perform a sensitivity of the simulated overtopping volumes to the interface method and the CFL number. This sensitivity is presented in a subsequent section.

2.1.3. Wave generation and absorption

Within waves2foam, wave generation and absorption in performed using relaxation zones. This technique weighs the computed and target (boundary) solution using a appropriate coefficient α_R according to the following:

$$\phi = \alpha_R \cdot \phi_{computed} + (1 - \alpha) \cdot \phi_{target} \tag{2.3}$$

Where ϕ is a fluid quantity. The weight coefficient α_R ranges from 0 at the boundary to 1 at the end of the relaxation zone towards the computational domain. Within waves2foam, several weight functions are available. Following the recommendations by Mayer et al. (1998) and A. Dimakopoulos and Higuera (2021) we employ the exponential function for that purpose, according to the following equation (Jacobsen et al., 2012):

$$\alpha_R(\chi_R) = 1 - \frac{e^{\chi_R^{3.5}} - 1}{e - 1} \tag{2.4}$$

where $\chi_R = x/L_R$ is the dimensionless horizontal position along the length L_R of the relaxation zone. This relaxation is performed explicitly in the fields of α (the VOF indicator function) and the velocity $\mathbf{u}$. The length of the relaxation zone needs to be at least one wave length of the peak period (L_p) for the waves to fully develop (Afshar, 2010; A. Dimakopoulos & Higuera, 2021; Moretto, 2020). For a comprehensive review of the method the reader is referred to A. Dimakopoulos and Higuera (2021).

2.2. OceanWave3D

While RANS solvers are accurate tools that have the ability to capture well the very complex physics of wave-structure interaction, they are computationally demanding. Importantly, the largest part of the wave transformation from the offshore to intermediate waters can be characterised by potential flow, since the influence of turbulence is limited. Therefore, potential flow models may be used for that region, instead of RANS. Such a model is OceanWave3D. This is a fully non-linear potential flow solver which is based on a flexible order finite difference discretization scheme. It is capable of providing accurate predictions of wave transformation close to the shore (Bingham & Zhang, 2007; Engsig-Karup et al., 2009). Being a potential flow solver, it is limited to a single valued free surface solution per space point, thus wave breaking is accounted for by adding dissipative terms on the free surface. Thus, this model is capable of providing stable solutions in a variety of coastal applications. For the wave generation and absorption, OceanWave3D employs the relaxation zone techniques, discussed in the previous section and has the capability to impose a flux boundary which approximates the paddle generation found in laboratory setups. This feature is particularly useful for validation purposes.

In order to simulate wave-structure problems efficiently, Paulsen et al. (2014) coupled OceanWave3D with OpenFOAM. This is done by exploiting the presence of relaxation zones within waves2foam. Essentially, the velocity field, pressure and free surface solution from OceanWave3D are mapped to the overlapping relaxation zone of the OpenFOAM domain and provide the appropriate boundary condition to the model. This coupling allows for the wave transformation from the offshore until the vicinity of the structure to be simulated in OceanWave3D. This effectively reduces the computational domain of OpenFOAM which results in significant decrease of computational times.

3

Validation

Prior to generating the numerical dataset, the model was validated against experimental data of overtopping over a vertical wall breakwater from the work of Dermentzoglou (2021), performed at the Hydraulic Engineering Laboratory of Delft University of Technology. Specifically, the correct reproduction of the water surface elevation, the overtopping volumes and wave energy spectrum were examined. For the first two variables only regular wave cases were considered. For the validation of the wave energy spectrum, wave gauge data from one irregular wave case were used. However, the irregular wave experimental data could not be used for validating the water surface elevation and overtopping volumes. While processing the experimental data from this case, some erroneous measurements in the wave paddle displacement signal were discovered, which prevented us from using the experimental paddle velocity to drive the model.

3.1. Experimental Data

The experimental setup consisted of a horizontal bottom flume with a length of 42 m., width of 0.8 m. and height of 1 m. The vertical wall breakwater was positioned at 33.33 m. offshore of the wave generation paddles. The wave paddles were equipped with second order generation capabilities and active reflection compensation (ARC) system. Wave gauges were used to measure water elevation in 6 locations across the flume. The overtopping volumes were measured using an overtopping box, positioned on the lee side of the structure. For the validation of the numerical model, 4 regular (prefix R) and 1 irregular (prefix IR) wave cases were used (Table 3.1). From the regular wave cases, 2 recorded overtopping while the rest, which no overtopping occurred, were employed only to validate the water level elevation.

Table 3.1: ID and parameters wave height ($H(m)$), wave period ($T(sec.)$), wave length ($L(m.)$), steepness (s), water depth to wave length ratio (d/L) of validation cases.

ID	$H(m)$	$T(s)$	$L(m.)$	s	d/L	Overtopped	Type
R12NA	0.12	1.57	3	4.00%	0.17	No	Regular Waves
R15NA	0.18	2.19	4.5	4.00%	0.11	Yes	Regular Waves
R24NA	0.16	2.2	4.57	3.50%	0.11	Yes	Regular Waves
R32NA	0.12	2.15	4	3.00%	0.13	No	Regular Waves
IR34J	0.11	3.40	7.3	1.50%	0.07	Yes	JONSWAP
IR34P	0.11	3.40	7.3	1.50%	0.07	Yes	Pierson-Moskowitz

3.2. Numerical Setup

As discussed earlier, key variables of interest in this study are the water elevation and overtopping. Hence, the OpenFOAM domain was divided into three regions of refinement as seen in Figure 3.2. Region 1 is defined as the refined region with a distance H, for regular wave cases, and H_{max}, for irregular wave cases, above and below the mean water level (i.e. 0) line. Cell size in this region is

equal to $\Delta x = H/16$. Region 2 corresponds to the area around the breakwater for which the cell size was chosen equal to $\Delta x = H/64$. The additional refinement is necessary in order to adequately resolve the overtopping wave above the crest of the structure and avoid the overestimation of the overtopping volumes due to numerical diffusion. This diffusion is introduced by the stretching of the overtopping wave flow height over a coarse grid (Moretto, 2020). Finally, region 3 represents all areas that are not of any particular interest, such as the atmosphere and the cell size is equal to $\Delta x = H/8$. For all regions, the cell aspect ratio is kept equal to 1 in order to avoid artificial breaking of the waves (Jacobsen et al., 2012; Patil, 2019). The length of the inlet relaxation zone was set to $1.5 * L_p$, where L_p is the wave length corresponding to the peak period Tp, following the recommendations of A. Dimakopoulos and Higuera (2021) and Jacobsen et al. (2012). L_p was calculated using the linear dispersion relationship. As it was previously described, the coupling algorithm within waves2foam interpolates the OceanWave3D solution to the OpenFOAM mesh. This entails the interpolation of a coarser grid (OceanWave3D) to a finer grid (OpenFOAM), which makes the accuracy of the procedure sensitive to the mesh resolution. Therefore, to adequately reproduce the evolution of the incident offshore waves and achieve good coupling between the two models, a relatively fine resolution horizontal mesh was used for OceanWave3D, with a size of $\Delta x = L_p/150$, according to Moretto (2020). Finally, the CFL number was set to 0.5. A simple sketch of the model domains is presented in figure 3.1.

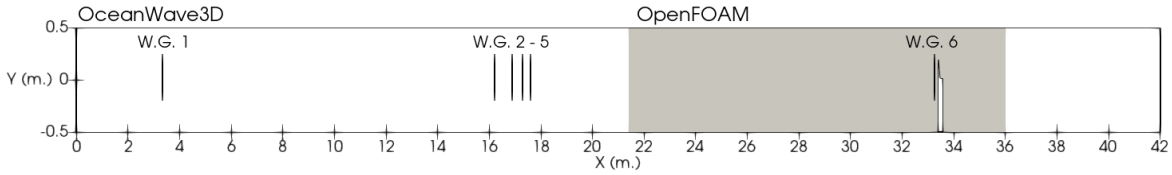

Figure 3.1: OceanWave3D and OpenFOAM computational domains together with the experimental wave gauge positions. Note that the vertical scale is exaggerated.

In order to replicate the experimental data the wave paddle velocities were applied as a boundary condition to OceanWave3D. The velocities were calculated from the recorded paddle displacements using a 4th order central difference scheme after the data were filtered using a 2nd order low pass Butterworth filter with a cutoff frequency at 2Hz. The same cutoff frequency was used for all cases and it was chosen so that all physical (e.g. the wave period T or in irregular waves at least $2 * T_p$) frequencies were included in the signal. All validation runs are performed using the isoAdvector scheme (Roenby et al., 2016; Roenby et al., 2017) for tracking the free surface position.

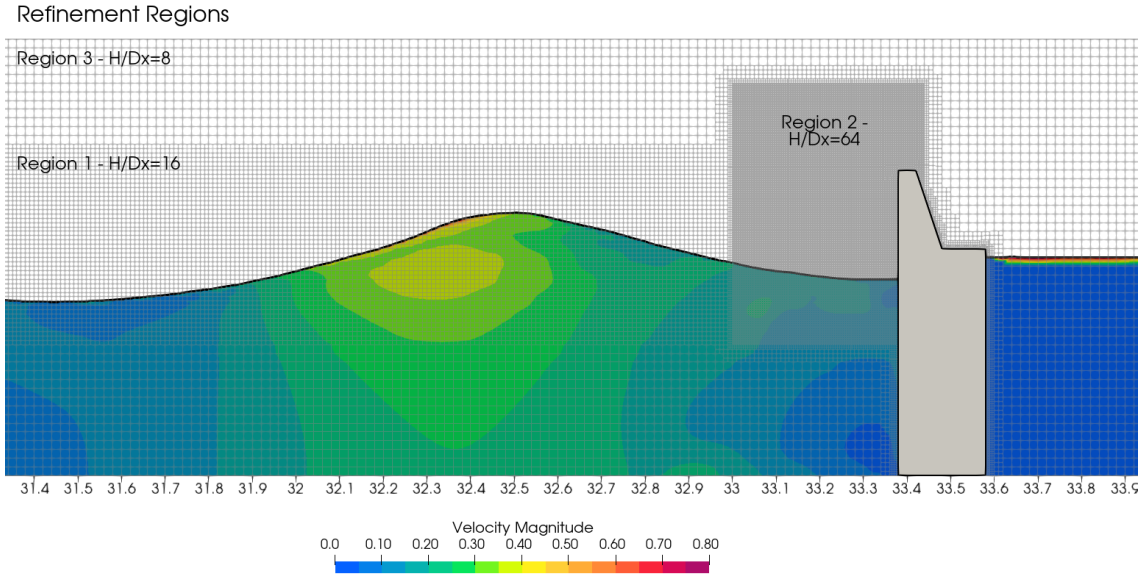

Figure 3.2: Mesh refinement regions

3.3. Reproduction of free surface elevation

In order to quantify the agreement between numerical and experimental results two metrics were used, namely the Pearson correlation coefficient (ρ) and the Root Mean Squared Error (RMSE). For every case, results from two wave gauges are presented, one in position $x = 17.6m.$ (WG5 of the experiment) and one in position $x = 33.33m.$ (WG6 of the experiment) which corresponds to the toe of the structure. Because of the coupled model, the OpenFOAM domain only extends from $x = 21.4m.$ to $x = 36m.$ (see Figure 3.1). Thus, only WG6 is used for the validation of the free surface elevation for this model. OceanWave3D covers the entire experimental domain and WG5 gauge was used for the same validation purpose. In this case, using WG6 to validate OceanWave3D would be meaningless since this wave gauge measures both the incident signal and reflected signal from the breakwater and this model only simulates the incident wave field.

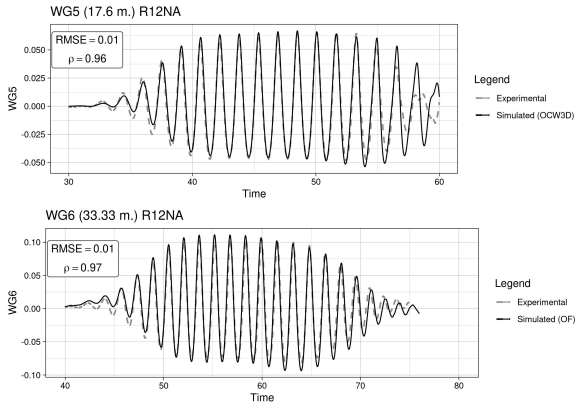

(a) Water level comparison, R12NA case

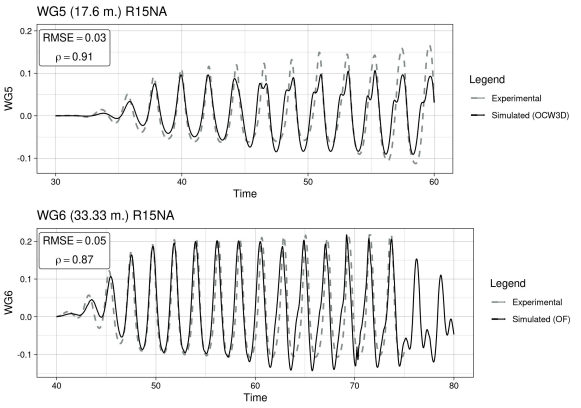

(b) Water level comparison, R15NA case

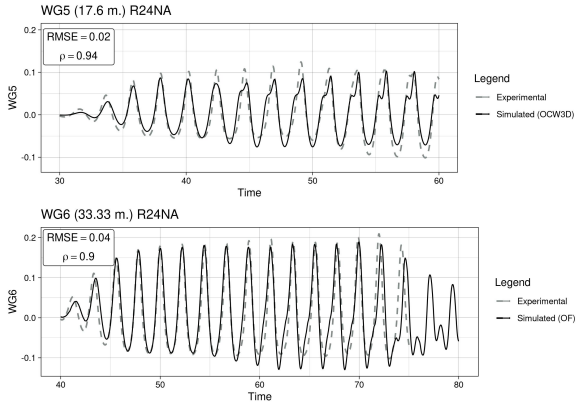

(c) Water level comparison, R24NA case

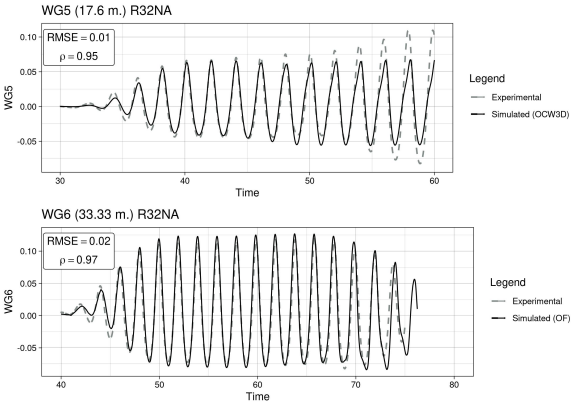

(d) Water level comparison, R32NA case

Figure 3.3: Water Level validation for 4 regular wave cases. For each subplot (a - d) top figure shows the OceanWave3D comparison and bottom the OpenFOAM comparison. The experimental measurements are denoted with grey color while the numerical results are denoted with black color.

The results are presented in Figure 3.3, showing a comparison of free surface elevation timeseries between experimental and simulated data. Overall, a very good agreement between experimental and numerical results has been achieved with low RMSE scores and high correlations between them. Despite that, two discrepancies can be observed. For the OceanWave3D results in subplots b and d the amplitudes of the experimental results increase after 50 seconds. This is due to the reflection which occurs in the laboratory flume. On the contrary, the numerical domain of OceanWave3D is open, i.e. a relaxation zone is prescribed at the outlet boundary to absorb the incident waves, therefore only the incident wave field is modelled, thus the wave amplitude remains constant. For this reason, OceanWave3D subplots only extend to 60 seconds. After that, the influence of the reflected wave is significant and the comparison is not valid. Secondly, on subplots b and c and for WG5, the waves produced by the numerical models show a second component around the wave crests with a period

much smaller than the wave period. This is due to the erroneous measurements of the wave paddle displacement in the laboratory data which are then inevitably transferred into the data.

3.4. Reproduction of overtopping volumes

Since the present study utilizes a numerical model to generate data of individual overtopping volumes, special care is taken to validate the performance of the model in this respect. However, experimental data of overtopping usually have a noisy signal due to the internal sloshing in the container being used for the measurements. Thus, in many cases it is difficult and unreliable to separate the cumulative signal into individual events. For this reason the validation is performed by comparing the cumulative overtopping volumes between experiments and numerical model. Those results are presented in figure 3.4 for cases R15NA and R24NA. A very good agreement in both cases has been achieved in terms of total volumes. However, there is a minor discrepancy in the profiles of the overtopping volumes, which is attributed to the noisy experimental signal, as discussed previously.

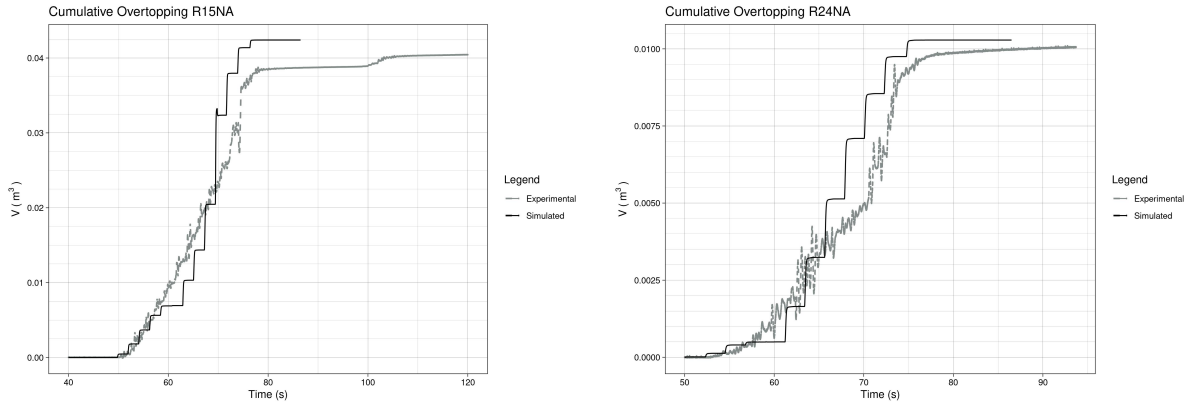

(a) Cumulative overtopping volume comparison, R15NA case

(b) Cumulative overtopping volume comparison, R24NA case

Figure 3.4: Cumulative overtopping volume validation. The experimental measurements are denoted with black color while the numerical results are denoted with grey color.

3.5. Wave energy spectrum and Reflection profile

The coupling between OceanWave3D and OpenFOAM is being performed through an interpolation of the incident wave field from the potential flow solver grid to the OpenFOAM relaxation zone nodes (Paulsen et al., 2014). If the OceanWave3D grid is very coarse, then the interpolation between the two model grids will have reduced accuracy. This is usually manifested in less wave energy being transferred from the OceanWave3D to the OpenFOAM domain (Moretto, 2020). To verify that the numerical models adequately preserve the boundary conditions we compute and compare the energy - frequency spectra between experimental and numerical results. To force the model, since the wave paddle signal cannot be used, we employed a spectral boundary condition with a JONSWAP shape and with the same integrated parameters as the experimental case IR34J. Figure 3.5 shows this comparison for the 6 measurement positions available. Wave gauges 1 - 5 cover the OceanWave3D domain while wave gauge 6 is located inside the OpenFOAM domain at the toe of the breakwater structure (as shown in Figure 3.1). A very good agreement between measured and numerical spectra can be observed, both in terms of significant wave height (H_s) and peak period (T_p). The only exception to this is wave gauge 6 where the experimental spectrum has lower energy ($H_s = 0.17m.$) than the numerical ($H_s = 0.22m.$). This discrepancy is attributed to faulty measurements of the wave gauge which are due to interference caused by the instrument's close proximity with the structure's vertical wall (i.e. 0.05 m.). Despite this, the calculated significant wave height is double the incident significant wave height, which is theoretically consistent with the fully reflective vertical wall structure. It should also be noted that the transfer of energy to the 2nd order super-harmonics is very well reproduced by both models.

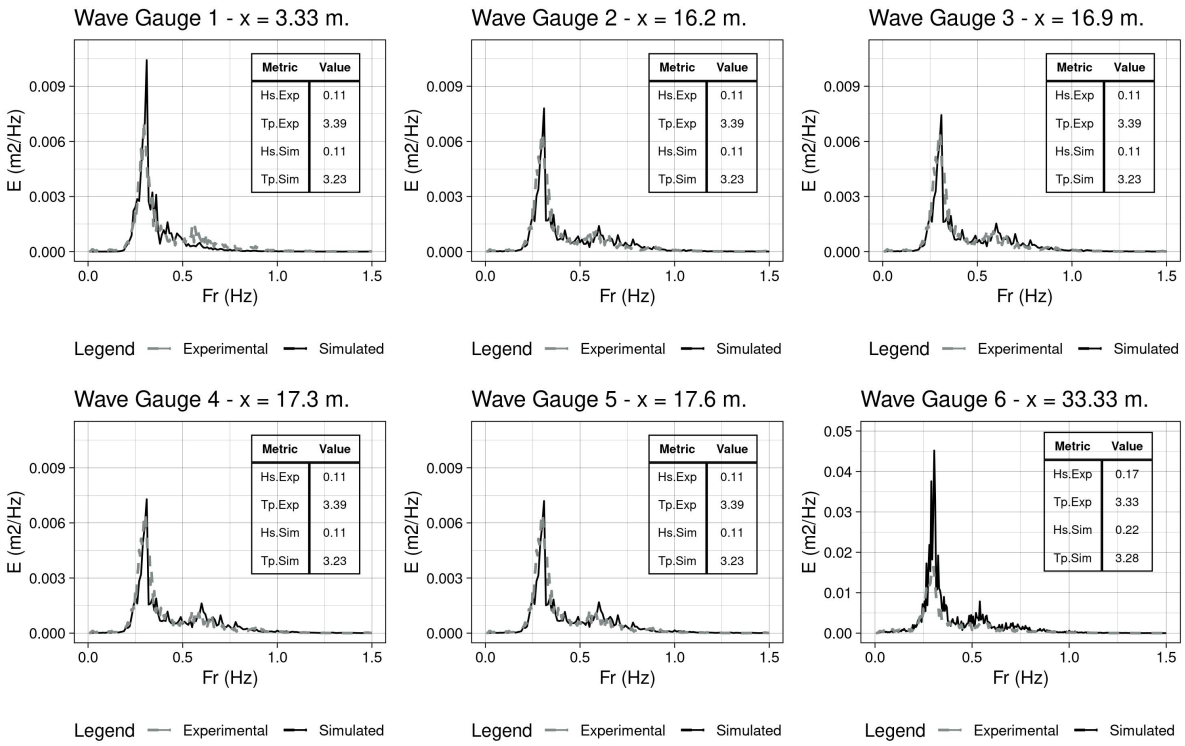

Figure 3.5: Experimental and Simulated Spectra comparison across the 6 wave gauge locations. Case IR34J

Additionally, we need to verify that the relaxation zone is able to effectively absorb the reflected waves within the OpenFOAM domain. To this aim we compare the simulated energy profile of the standing wave which forms at the front of the structure with the theoretical expression for a fully reflective wall, given by Goda and Suzuki (A. S. Dimakopoulos et al., 2016; Goda & Suzuki, 1976) (Equation 3.1)

$$H_s(x) = 4\sqrt{\int_0^\infty (1 + 2cos(2k(f)x) + 1)S_{inc}(f)df} \tag{3.1}$$

where $H_s(x)$ is the significant wave height (incident and reflected) as a function of the distance from the structure x, S_{inc} is the energy density of the incident spectrum and k is the wave number. It should be noted that this relationship only holds for linear waves and the wave numbers k where calculated by solving the linear dispersion relationship for every frequency in the discretised incident spectrum. Figure 3.6 shows a comparison between theoretical and numerical results of the significant wave height divided by the incident significant wave height ($H_s(x)/H_{s,inc}$) as a function of the distance from the structure. This comparison is done for two incident spectral shapes, JONSWAP with a peak factor $\gamma = 3.3$ and Pierson-Moskowitz. For both cases a very good agreement between the numerical and the theoretical results is achieved, which proves the model's ability to correctly absorb the reflected waves and avoid unwanted internal reflections in the computational domain which could contaminate the overtopping results.

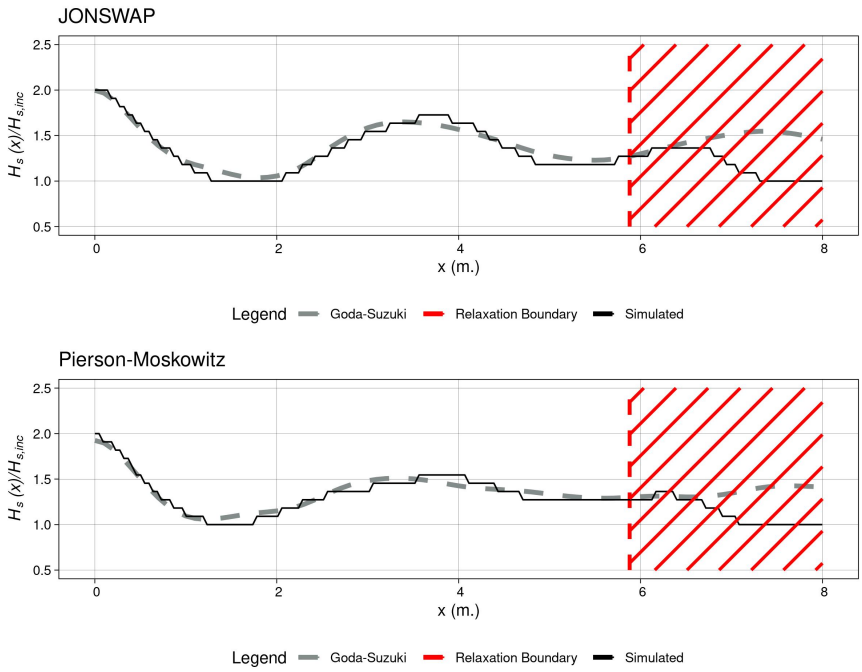

Figure 3.6: Significant wave height to incident significant wave height ratio ($H_s(x)/H_{s,inc}$) as a function of the distance from the structure (x axis) compared with the theoretical solution from Goda-Suzuki (Goda & Suzuki, 1976). The red dashed region marks the inlet relaxation zone of the OpenFOAM domain. Case IR34

3.6. isoAdvector vs MULES

For the validation presented during the previous chapter the isoAdvector scheme was employed to resolve the interface position. As mentioned during chapter 2, this scheme has some favourable properties compared to MULES. To verify those results it was decided to repeat one of the validation cases (R15NA) with interFoam and compare the results. Initially, the two methods were compared using the same CFL condition (CFL=0.50). Figure 3.7 presents the free surface elevation and velocity fields of a single time step for the two methods. isoAdvector is able to produce a smooth interface despite the presence of a sharp crest. On the contrary, the interface produced by MULES exhibits the distinct numerical wiggles produced by the method. Moreover, it is observed that this results in increased velocities close to the free surface. Larsen et al. (2019) indicate that the interface compression algorithm used in MULES to keep the interface sharp, is likely responsible for this behaviour.

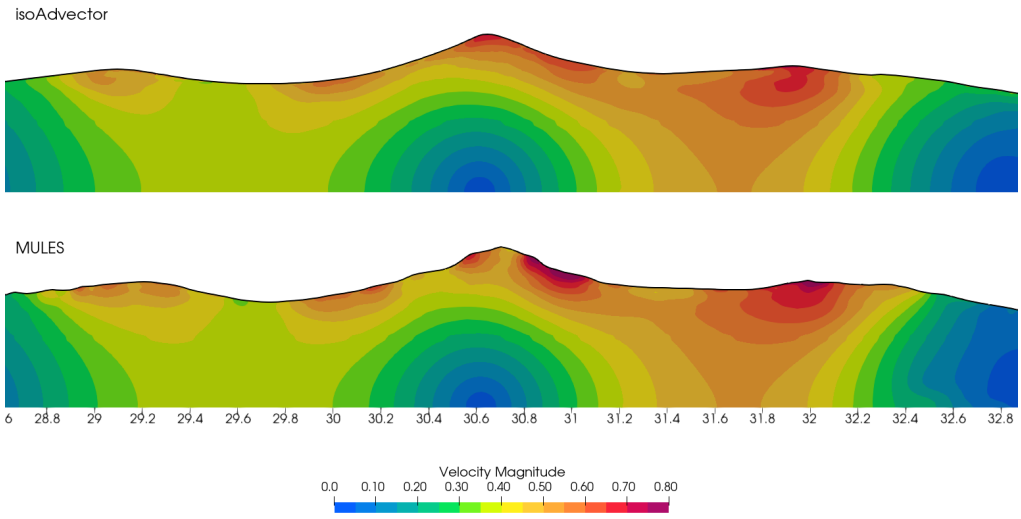

Figure 3.7: Interface comparison between isoAdvector (top) and MULES (bottom). For both simulations a CFL of 0.50 was used.

Figure 3.8 presents the comparison between the two methods in terms of cumulative overtopping volumes. It appears that the two algorithms perform similarly.

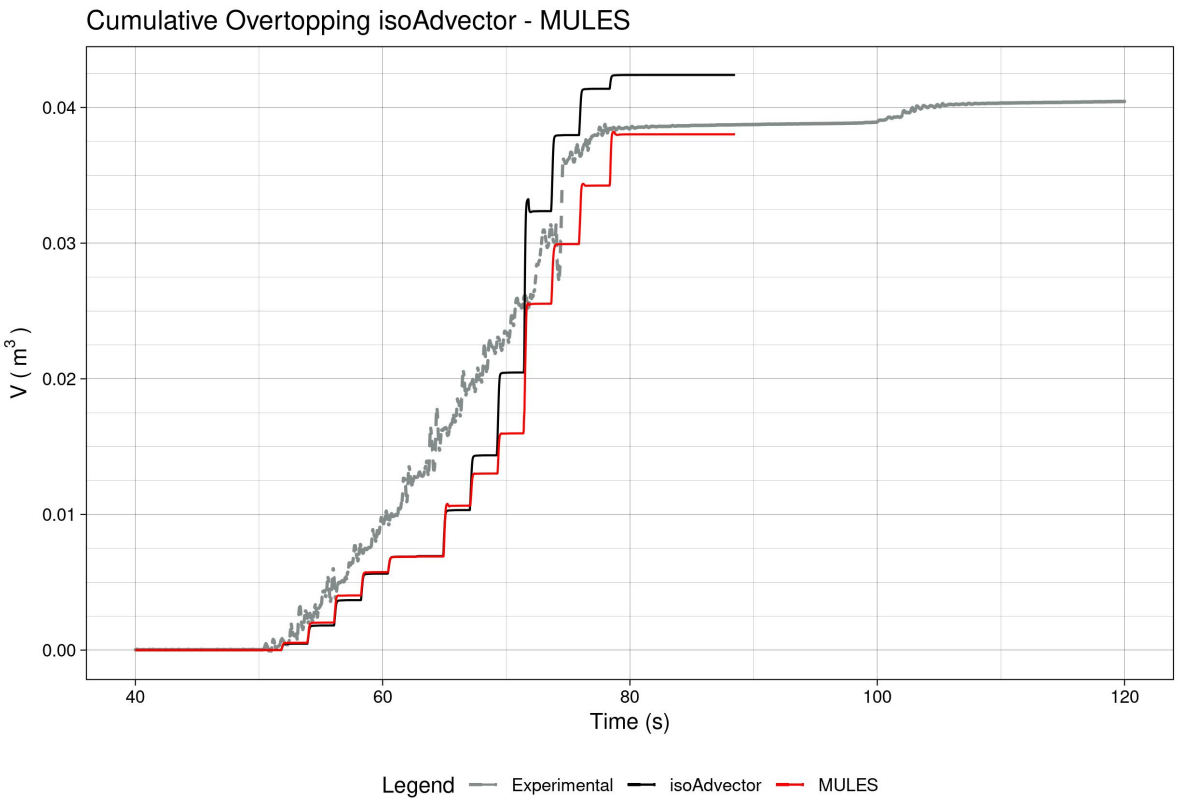

Figure 3.8: Cumulative overtopping volume comparison between isoAdvector and MULES for CFL=0.50.

In addition to the above comparison, a sensitivity based on the CFL condition was conducted for both methods. It is observed that overtopping, when calculated using isoAdvector is less sensitive to the choice of the CFL number (Figure 3.9a). On the contrary it was found that overtopping calculations using MULES are more affected by the time step (Figure 3.9b). This is probably caused by the fact that the sharpness of the interface is greatly affected by the choice of CFL, as documented from Larsen et al. (2019), which is very important in accurately capturing the position of the free surface when a wave is overtopping. However, further investigation of this subject falls outside of the scope of the present study.

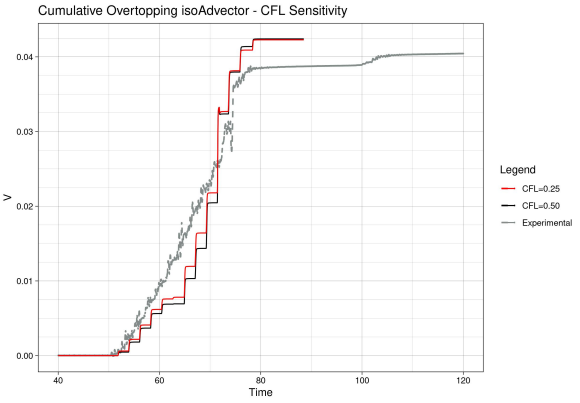

(a) Cumulative overtopping volume sensitivity for CFL values of 0.25 and 0.50 using the isoAdvector method.

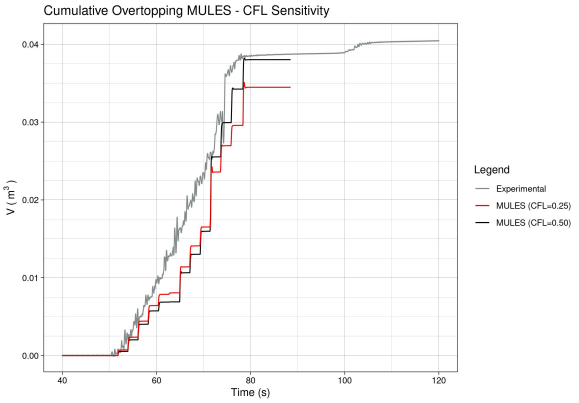

(b) Cumulative overtopping volume sensitivity for CFL values of 0.25 and 0.50 using the MULES method. isoAdvector results for CFL=0.50 are also presented for comparison.

3.6.1. Sensitivity of overtopping to grid refinement

In addition to the validation of the model against the measured cumulative overtopping volumes, we conducted a sensitivity on the grid refinement around the breakwater region (Region 2 of figure 3.2) with the aim of examining it's influence in overtopping. Specifically, two additional simulations where run for case R15NA with Region 2 refinement of $\Delta x = H/16$ and $\Delta x = H/32$. Figure 3.10 presents the results compared against the validation case ($\Delta x = H/64$). As expected, the coarser refinement of $\Delta x = H/16$ results in a overestimation of the cumulative overtopping volumes, because of the numerical diffusion introduced by the stretching of the overtopping wave flow height over the coarse grid (Moretto, 2020). However, when the individual events are examined more closely, it can be observed that the initial, smaller events are underestimated for the 2 coarser grids. This may be the result of grid refinement being comparable to the height of the flow above the breakwater, which leads to reduced measured overtopping. This is not observed in the case of $\Delta x = H/64$, which resolves all overtopping events adequately. Overall, the coarser refinements with $\Delta x = H/16$ and $\Delta x = H/32$ overestimate the larger overtopping events and underestimate the smaller ones. The finer refinement with $\Delta x = H/64$ is able to accurately reproduce the measured overtopping volumes across all scales. Further refinement of the grid would increase the computational cost of the model to impractical levels, by increasing the total cell count and by decreasing the simulation time step. Therefore, for the present study a refinement of $\Delta x = H/64$ for Region 2 is considered adequate for accuracy and computational efficiency.

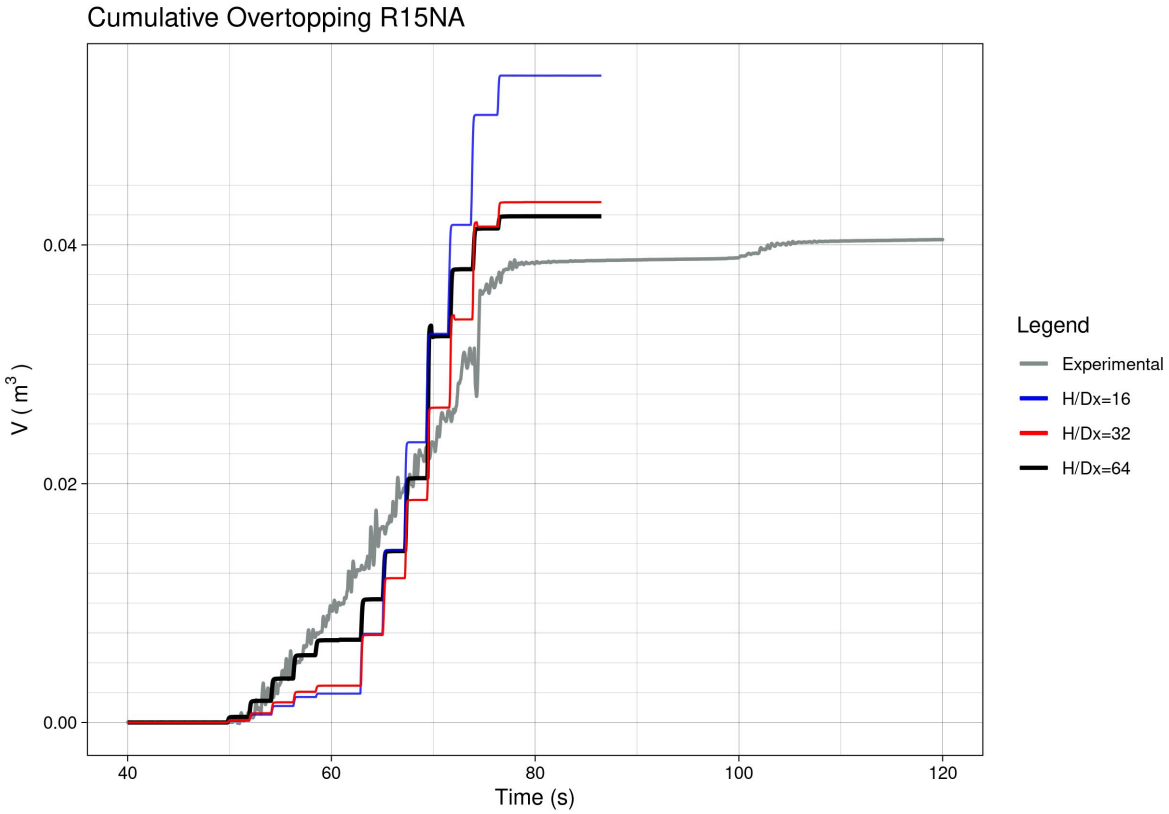

Figure 3.10: Cumulative overtopping volume sensitivity for grid resolution around the breakwater (Region 2 of figure 3.2). Case R15NA

4

Numerical Experiments and Results

To generate the numerical data set required for the statistical analysis of individual overtopping volumes, a total of six cases were simulated, with the boundary conditions given in Table 4.1. For each set of boundary conditions, two spectral shapes were tested, namely a JONSWAP with peak factor of $\gamma = 3.3$ and a Pierson-Moskowitz (i.e. peak factor of 1). In order to retrieve reliable overtopping statistics we aimed to simulate at least 1000 waves for every case (Romano et al., 2015; Williams et al., 2014). The number of total simulated waves, the number of overtopping waves (N_{ow}) and the percentage of overtopping waves (P_{ow}) are given in Table 4.1 for every simulated case. The simulations were run on a desktop computer with a 6 core Ryzen 5600X CPU. For each case the simulation time was approximately 3 weeks. In each simulation the water surface elevation was sampled at the position of the wave gauges. Additionally in OpenFOAM, the water surface elevation was sampled every 5 cm. and the overtopping discharge was measured at each time step. Figure 4.1 presents the timeseries of the incident water surface elevation measured at location $x = 33.3m$. (subplot a) and the timeseries of the overtopping discharge (subplot b) for case IR11T.

Table 4.1: Numerical Experiments

Scenario	$H_s(m)$	$T_p(s)$	Spectra	Waves	N_{ow}	P_{ow}	R_c/H_s
IR11	0.11	2.43	JONSWAP	1371	195	0.14	0.91
IR11_PM	0.11	2.43	P-M	1193	129	0.11	0.91
IR11T	0.11	3.48	JONSWAP	1165	276	0.24	0.91
IR11T_PM	0.11	3.48	P-M	1225	281	0.23	0.91
IR15	0.15	3.48	JONSWAP	1467	225	0.15	1.33
IR15_PM	0.15	3.48	P-M	1073	103	0.10	1.33

For the simulation of the above cases, the same model parameters were used, as described in the validation section, with the exception of the CFL number. During the long simulations it was observed that instabilities seldom occurred in the water-air interface, especially in the transition regions between different mesh refinements. These instabilities are known in the literature as spurious or parasitic currents and can be caused by an improper numerical discretization of the gravitational force in the momentum equations (Moeller, 2021). These spurious currents can appear at random and are exacerbated by steep waves and by the sharp water - air interface produced by isoAdvector(Larsen et al., 2019). In an effort to limit the effect of such currents in our simulations, the CFL number was reduced to 0.25.

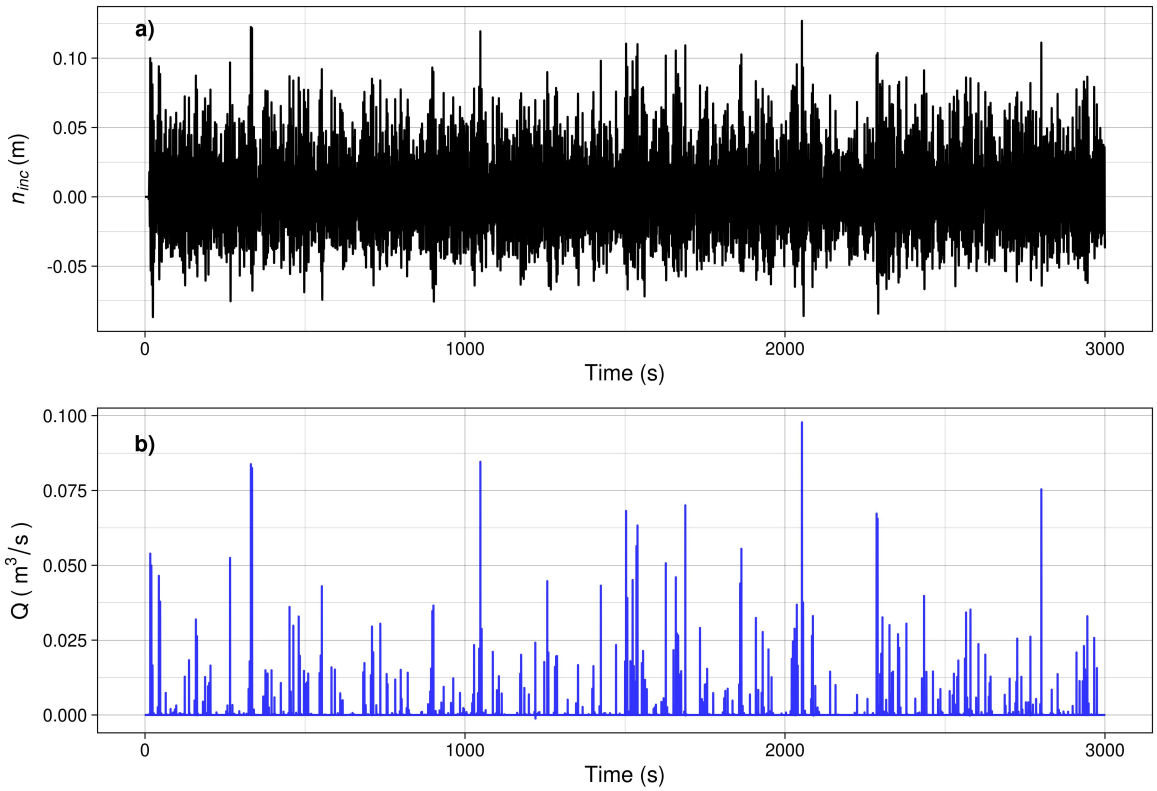

Figure 4.1: a) Timeseries of incident water surface elevation measured at $x = 33.3m$. measured from OceanWave3D and b) timeseries of overtopping discharge. Case IR11T

4.1. Comparison of results with EurOtop

To gain additional confidence in the numerical results, these were compared against the empirical equations from EurOtop manual (van der Meer et al., 2018) in terms of typical design quantities, namely the average overtopping discharge q, the percentage of overtopping waves P_{ow} and the maximum overtopping volume V_{max}. For cases IR11 and IR11_PM the equation for non-influencing foreshore (Equation 4.1) is used to calculate q, while for all other cases, because of the shoaling present due to longer periods and higher H_s, the equation for influencing foreshore and non-impulsive waves (Equation 4.2) is used.

$$\frac{q}{\sqrt{gH_{m0}^3}} = 0.047e^{-(2.35\frac{R_c}{H_{m0}})^{1.3}} \tag{4.1}$$

$$\frac{q}{\sqrt{gH_{m0}^3}} = 0.05e^{-(2.78\frac{R_c}{H_{m0}})} \tag{4.2}$$

In addition to the mean estimate of the average overtopping discharge, the 95% confidence intervals are calculated. To do so, the equation parameters are assumed to follow a normal distribution as proposed by van der Meer et al. (2018). The percentage of overtopping waves for non-impulsive conditions assumes a Rayleigh distribution according to Equation 4.3.

$$\frac{N_{ow}}{N_w} = e^{-1.21(\frac{R_c}{H_{m0}})^2} \tag{4.3}$$

Additionally, according to EurOtop manual, the individual overtopping volumes follow a two-parameter Weibull distribution expressed as:

$$P_V = 1 - e^{-(\frac{V}{a})^b} \tag{4.4}$$

where b is the shape parameter which depends on the incident wave conditions and a is a scaling parameter calculated according to $a = (\frac{1}{\Gamma(1+\frac{1}{b})})(\frac{qT_m}{P_{ow}})$. For cases IR11 and IR11T parameter b was taken equal to 0.66 while for the other cases it was set equal to 0.85. Based on the above, the maximum overtopping volume V_{max} can be calculated as a function of the number of waves overtopping N_{ow} according to Equation 4.5:

$$V_{max} = aln(P_{ow})^{1/b} \tag{4.5}$$

Figure 4.2 shows a good overall agreement between the empirical formulas and the numerical results, for all three variables. Specifically, the average simulated overtopping discharge falls within the 95% confidence intervals, predicted by EurOtop (Figure 4.2a). The empirical Weibull distribution is able to predict the simulated maximum overtopping volumes with very good accuracy (Figure 4.2c). The largest deviation is observed in the estimation of the percentage of overtopping waves and cases IR11, IR11T where the EurOtop formula provides a result which is twice the simulated result. This discrepancy could be the result of the test duration and the choice of the seeding value used for the random phasing in the decomposition of the spectra. As discussed in Williams et al. (2014) and Romano et al. (2015) the percentage of overtopping waves can vary between tests of the same wave conditions. However, this type of error affects q to a much smaller extent (Romano et al., 2015). This phenomenon is caused by the different sequences of random waves generated by decomposing the boundary spectrum. Additionally, EurOtop does not provide confidence intervals for the parameters of the above formulation, therefore the significance of the deviation cannot be assessed. Based on the agreement with the other parameters, this result is considered acceptable.

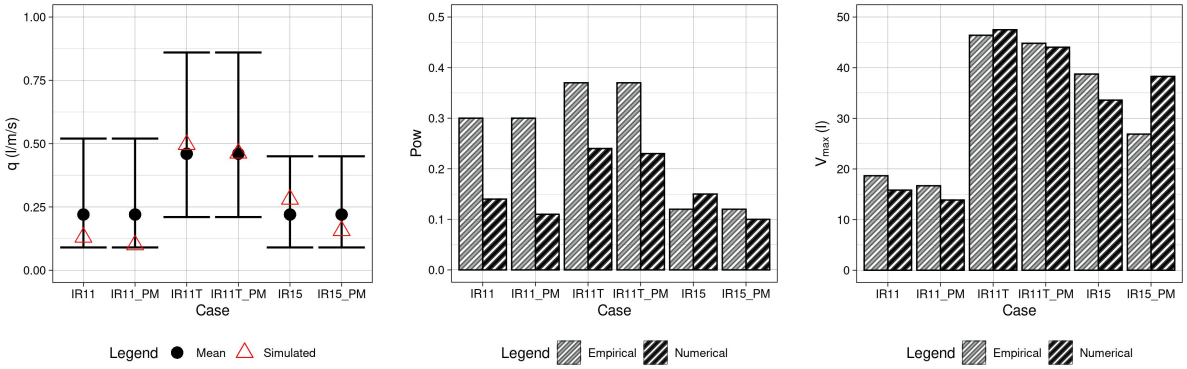

(a) Mean overtopping discharge. Error bars denote upper and lower 5% quantiles.

(b) Percentage of overtopping waves.

(c) Maximum individual overtopping volume.

Figure 4.2: EurOtop 2018 comparison with numerical results

Finally, the distribution of the individual overtopping volumes is compared against EurOtop (Equation 4.4). Figure 4.3 presents the probability plot of the simulated and EurOtop distributions. According to this technique, the vertical axis (probability axis) is scaled using the inverse of the theoretical Cumulative Distribution Function (CDF). In doing so, the theoretical distribution appears as a straight line in the plot which aids the visual comparison between distributions. A good agreement between the EurOtop (Equation 4.4) and simulated distributions is observed for cases IR11 and IR11T. In both cases, only small deviations are found for the higher percentiles. On the contrary, case IR_15 shows a deviation around the tail. Specifically, the simulated distributions predict a higher probability of exceedance for a given overtopping volume above the 75% percentile for the JONSWAP case and 92% percentile for the P-M case. Additionally, it is noted that no notable difference can be observed between the two examined spectral shapes for all cases.

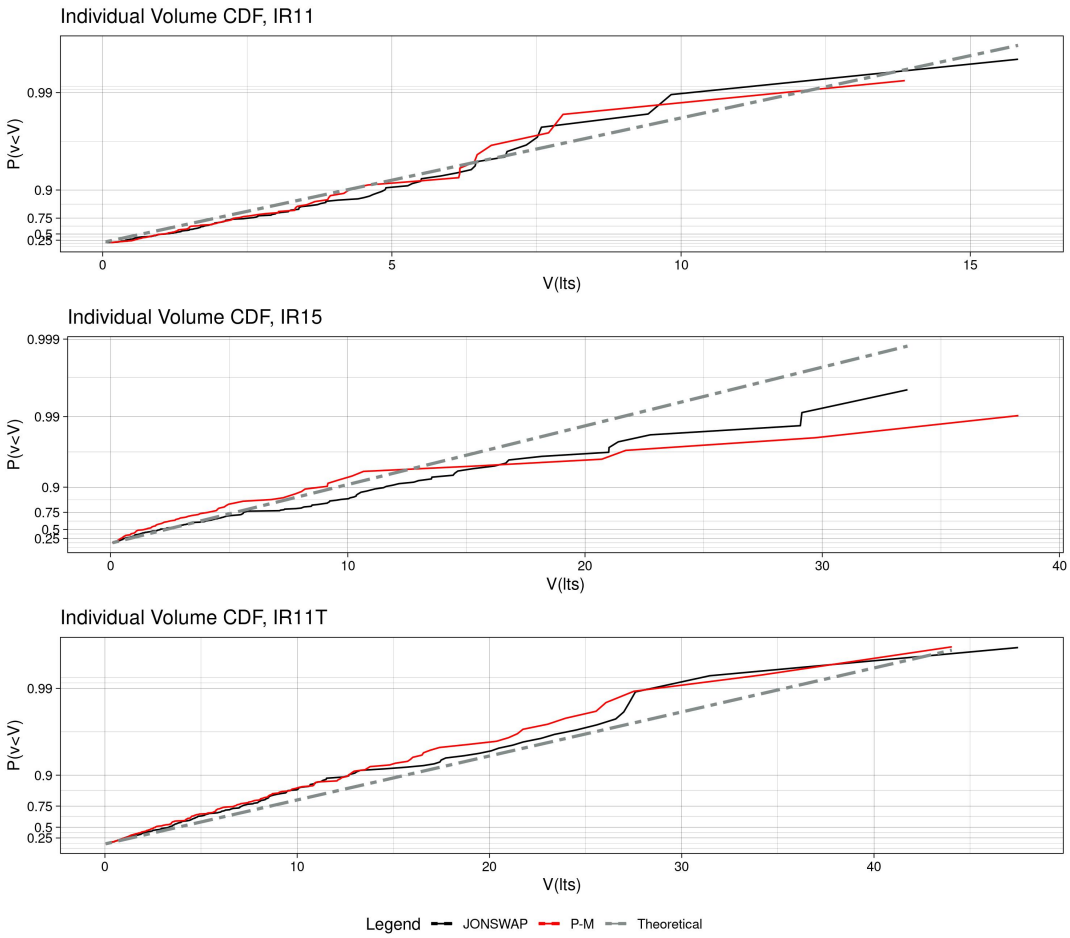

Figure 4.3: Individual overtopping volume distribution. Comparison between simulated and EurOtop 2018 distributions

5

Dependencies of individual overtopping volumes

When examining the dependencies of overtopping volumes on wave characteristics, investigating the contribution of the incident wave height H_{inc} is a reasonable first step. In this analysis, the incident wave conditions are derived from the simulations performed with OceanWave3D, since this model simulates only the undisturbed wave field without the influence of the structure. This method is opted so we do not have to rely on reflection analysis procedures which are likely to be based on linear wave theory (e.g. Zelt and Skjelbreia (1992)). It is reminded that the OceanWave3D model is run in a coupled manner with OpenFOAM and the incident irregular wave field is used to force the OpenFOAM part of the simulation with the structure in place. Figure 5.1 shows the incident wave height at the toe of the breakwater ($x = 33.3m.$) and the corresponding overtopping volumes, both of which are normalised by their respective maximum values.

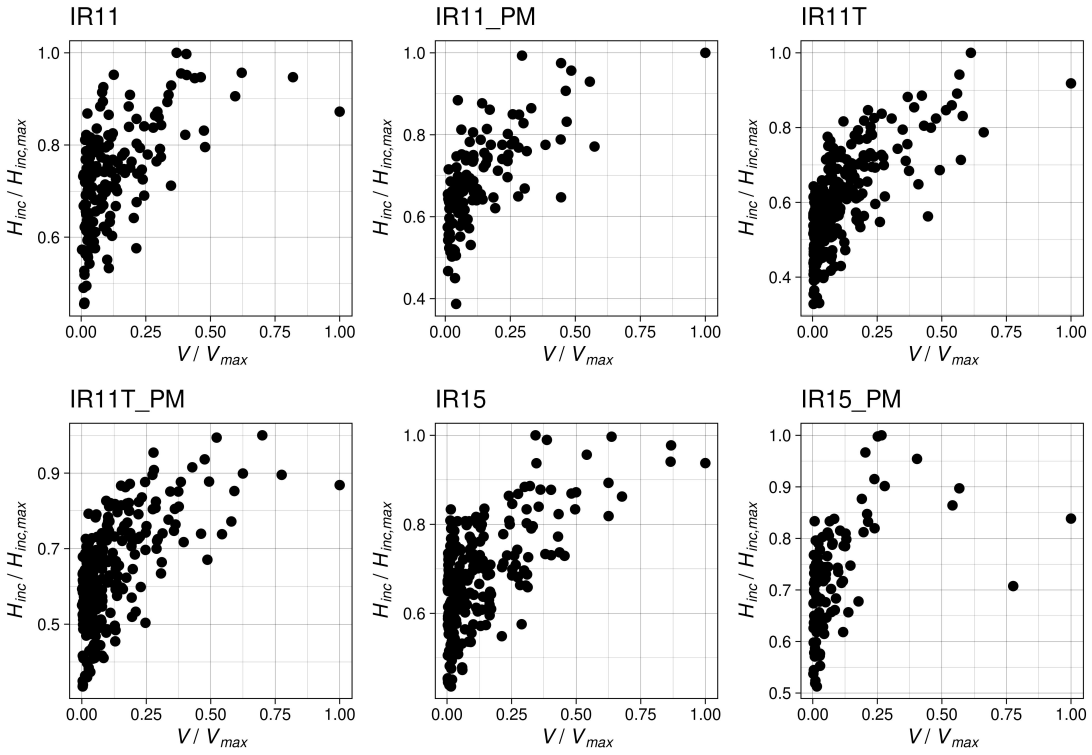

Figure 5.1: Scatter plot between incident wave height H_{inc} and individual overtopping volumes V normalised by their maximum values

From all cases it can be observed that incident wave heights above a threshold can produce significantly different overtopping volumes. For example, in case IR11T, waves equal to 80% of their maximum produce events which range from roughly 20% to 62% of the maximum overtopping volume. It should be noted that using a different normalising value, for example the average of the variables instead of the maximum (see Appendix A.2), does not alter these relationships. To further investigate this phenomenon, we plot the water surface elevation time series before and after two overtopping events with the same incident wave height but with different overtopping volumes. Figure 5.2 presents two realisations of an incident wave, from the same simulation, which is approximately equal to $H_{inc}/H_{inc,max} \approx 80\%$. In case $a)$ the same wave height produces three times higher overtopping volume than case $b)$. In the same figure, the total (incident + reflected) water surface elevation, derived from the OpenFOAM simulation, is plotted together. From this figure it is evident that the difference between the two cases is the horizontal asymmetry of the wave. Specifically, in case $a)$ the wave has a higher crest height and a higher trough, than the one depicted in case $b)$. This finding persists across all cases (see Appendix A.1).

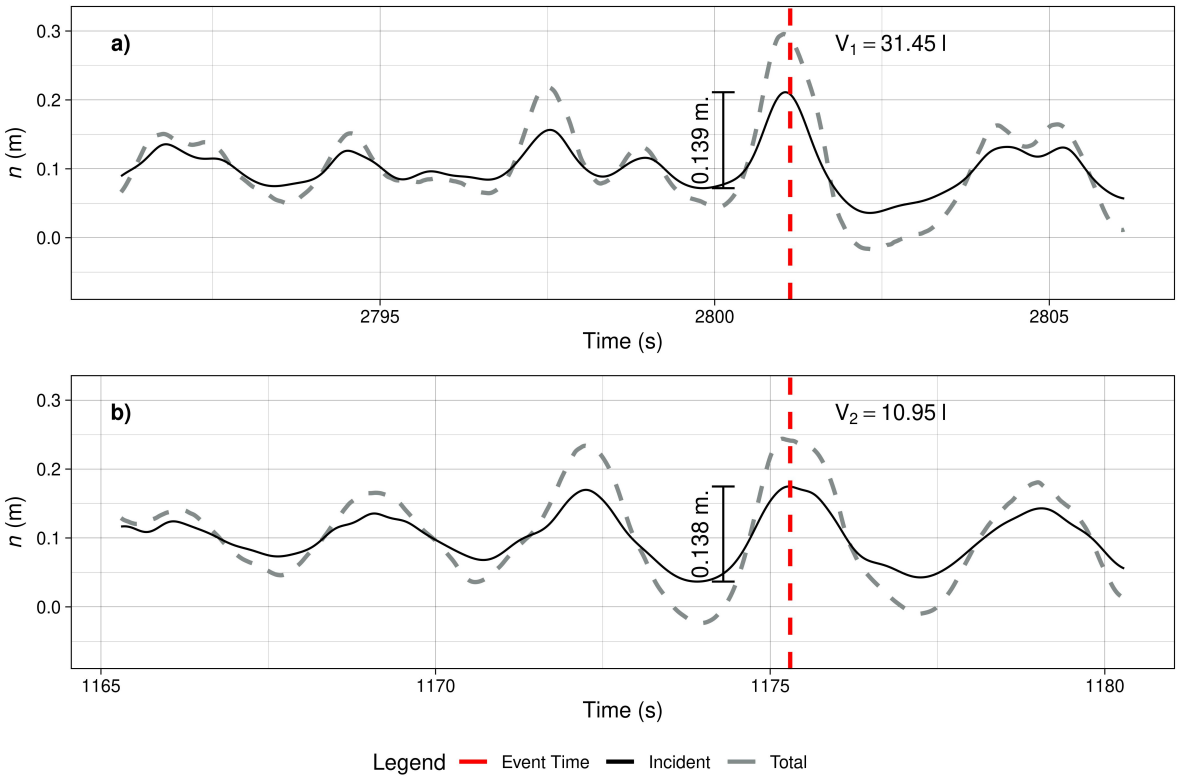

Figure 5.2: Incident and total water surface elevation at the toe of the breakwater for two realisations of an incident wave $H_{inc}/H_{inc,max} \approx \%80$ with different overtopping volumes. The incident signal is derived from OceanWave3D and the total (incident + reflected) from OpenFOAM. Case IR11T

This result indicates that the wave crest level n_c will correlate better with the overtopping volumes. This is verified in Figure 5.3, were the incident wave crest level, for the same flume location, is plotted along with the corresponding volumes. A strong correlation is observed between the two. Importantly, it appears that incident waves with the highest crest levels will produce events with the maximum, or the second maximum overtopping volume. In addition to the above, the scatter plot between the total crest level, derived from the combined incident and reflected signal of OpenFOAM, with the corresponding volumes is presented in Appendix A.3, Figure A.8 and demonstrates the same strong correlation between the two, with the exception that the scatter is noticeably decreased.

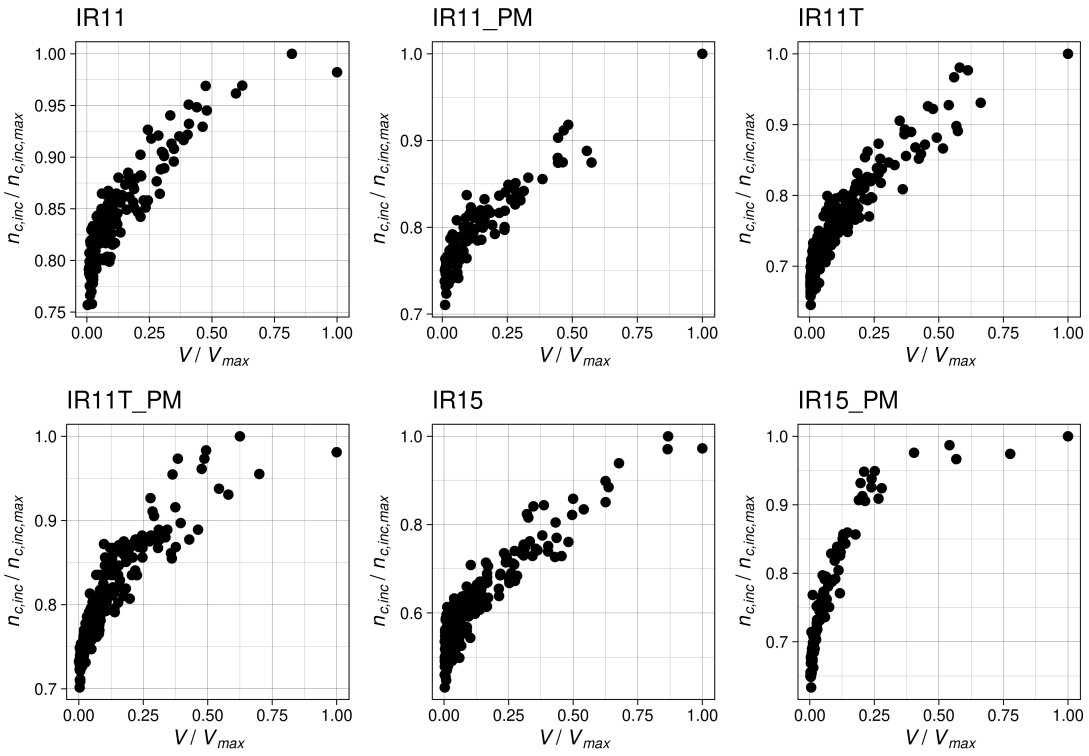

Figure 5.3: Scatter plot between incident wave crest $n_{c,inc}$ and individual overtopping volumes V normalised by their maximum values

To quantify the dependence of the incident wave height and crest level with the overtopping volumes, the Spearman correlation coefficient (Spearman, 1904; “Spearman Rank Correlation Coefficient”, 2008) is calculated between the variables. Again, the measurement location for this analysis is the toe of the breakwater ($x = 33.3m.$). Additionally, other variables of interest are examined, namely, the wave period T, the wave length L (which is calculated using the linear dispersion relationship), the wave trough level n_t and the wave steepness ϵ, as defined by $\epsilon = H/L$. These are calculated for both the incident (Table 5.1) and the total (Table 5.2) wave conditions.

Table 5.1: Spearman Correlation of individual overtopping volumes with incident wave parameters

Scenario/Spearman Rank	H_{inc}	T_{inc}	$n_{t,inc}$	$n_{c,inc}$	L_{inc}	ϵ_{inc}
IR11	0.58	0.14	-0.1	0.89	0.14	0.42
IR11_PM	0.71	0.05	-0.31	0.9	0.05	0.56
IR11T	0.7	0.11	-0.15	0.94	0.11	0.58
IR11T_PM	0.6	0.1	-0.08	0.96	0.1	0.49
IR15	0.55	-0.13	0.09	0.9	-0.13	0.49
IR15_PM	0.59	-0.16	-0.02	0.97	-0.16	0.49

Table 5.2: Correlation of individual overtopping volumes with total (incident + reflected) wave parameters

Scenario/Spearman Rank	H	T	n_t	n_c	L	ϵ
IR11	0.61	0.09	-0.14	0.98	0.09	0.46
IR11_PM	0.7	0.05	-0.32	0.98	0.05	0.53
IR11T	0.64	0.1	-0.15	0.97	0.1	0.51
IR11T_PM	0.62	0.09	-0.07	0.97	0.09	0.44
IR15	0.6	-0.15	0.12	0.99	-0.15	0.48
IR15_PM	0.69	-0.12	-0.03	0.99	-0.12	0.47

In all cases the highest rank correlation is found for the wave crest level. For the incident wave crests the correlations with the individual overtopping volumes range between $0.87 - 0.94$ while for the total (incident and reflected) wave crests they range between $0.97 - 0.99$, showing almost perfect correlation. The incident wave height correlations appear lower, but still remain significant, showing values between $0.55 - 0.70$. Moreover, the steepness of the waves correlates well with overtopping. On the contrary, the wave period and the wave length show insignificant correlations.

While the Spearman Rank is a convenient metric to quantify correlations, it cannot fully describe the dependence structure between two variables. For example, variables can have different correlation in the upper quantiles from the lower quantiles (for a wider discussion on the pitfalls of using only correlation metrics to characterise dependence the reader can refer to Embrechts et al. (2002)). To fully characterise the dependence structure between two variables we have to examine their joint probability. To do so, we will employ Copula functions. Copulas are joint distributions with uniform margins. They were introduced by *Sklar* (Sklar, 1959), which showed that any joint distribution can be expressed as a combination of it's marginals and a copula function. This approach, effectively allows the study of the dependence structure without the influence of the marginal distributions. Based on Sklar's theorem the joint probability between the incident wave crest level n_{inc} and the individual overtopping volumes can be written as:

$$F_{n_{inc},V}(n_{inc}, V) = C(F_{n_{inc}}, F_V) \tag{5.1}$$

where C is the copula function and $F_{n_{inc}}$ and F_V are the marginal distributions of the incident crest and individual overtopping volumes respectively. When visualising copulas, it is often beneficial to transform the variables to the standard normal space. In doing so, differences in the behaviour of the tails can be better illustrated.

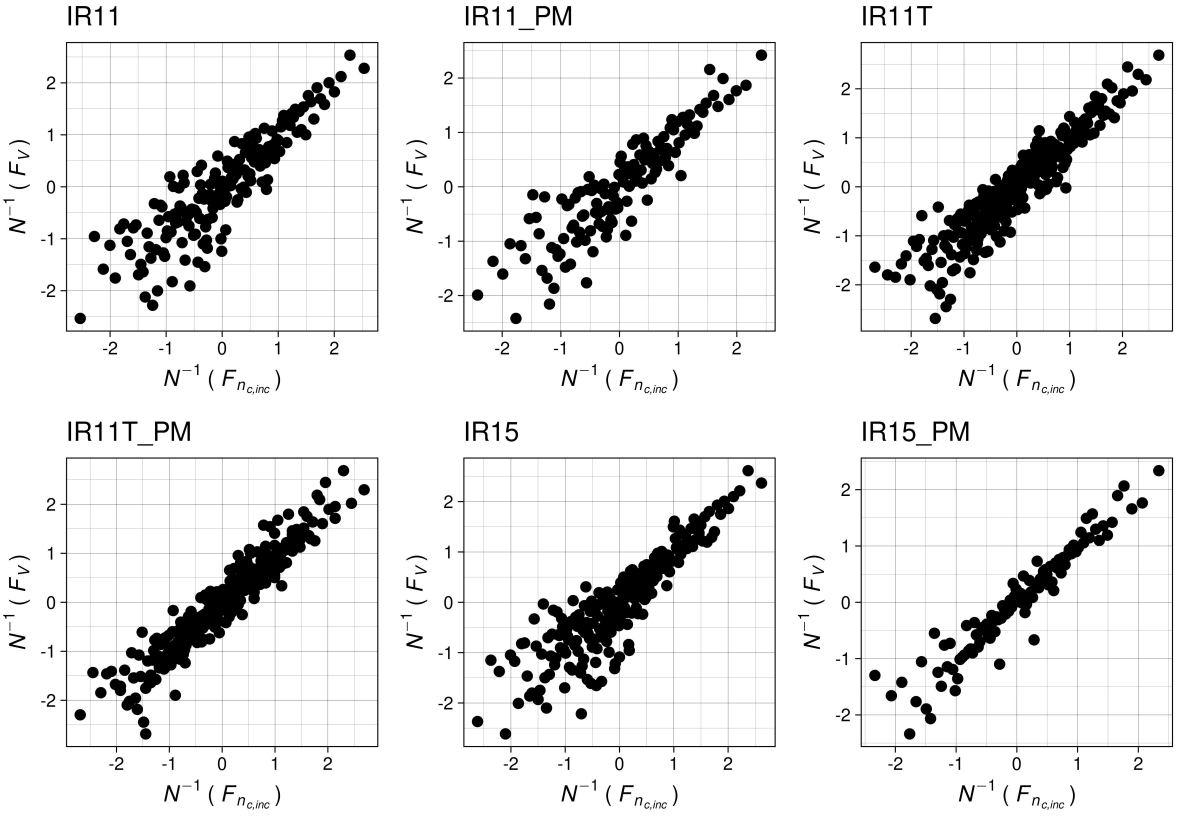

Figure 5.4: Empirical copulas between incident wave crest n_{inc} and individual overtopping volumes

Figure 5.4 presents the normalised copulas of overtopping volumes and wave crests for all cases. N^{-1} denotes the inverse standard normal distribution. From the figure it is observed that the scatter of events around the lower and upper tail differs. Specifically, for the higher events the scatter decreases, indicating a higher correlation between high events. The opposite holds for the lower tails. In practical

terms, this means that high wave crests usually occur together with high overtopping volumes. A metric to assess this tail asymmetry is given in the form of semi-correlations, by Joe (2014). These are simply defined as the Pearson Correlation of the normalised joint upper and lower quadrant of the variables and are given by the following equations:

$$\begin{aligned}\rho_N^+ &= Cor[N^{-1}(F_{n_{inc}}), N^{-1}(F_V)|N^{-1}(F_{n_{inc}}) > 0, N^{-1}(F_V) > 0] \\ \rho_N^- &= Cor[N^{-1}(F_{n_{inc}}), N^{-1}(F_V)|N^{-1}(F_{n_{inc}}) < 0, N^{-1}(F_V) < 0]\end{aligned} \tag{5.2}$$

The semi-correlations can be calculated for the other two quadrants in the same way, but are not of interest in this study. The semi-correlations for all cases are presented at Table 5.3. Note that the $+$ superscript denotes semi-correlation of the upper quadrant and the $-$ superscript denotes semi-correlation of the lower quadrant. Additionally, ρ_N denotes the Pearson correlation calculated for all data. The estimated semi-correlations confirm that indeed, a very strong correlation ($\rho_N^+ > 0.88$) exists in the upper tails for all cases. However, the lower tails do not exhibit such a uniform correlation pattern. Specifically, while in all cases $\rho_N^+ > \rho_N^-$, cases IR11T, IR11T_PM and IR15_PM show notably higher ρ_N^- than the rest.

Table 5.3: Correlation and semi-correlations between wave crest and overtopping volumes

Scenario	ρ_N	ρ_N^+	ρ_N^-
IR11	0.90	0.89	0.52
IR11_PM	0.91	0.88	0.58
IR11T	0.95	0.9	0.7
IR11T_PM	0.96	0.88	0.83
IR15	0.91	0.93	0.52
IR15_PM	0.97	0.95	0.81

A more rigorous description of the concurrence of high events can be found in the notion of tail dependence. Let us consider two variables, the incident wave crest n_{inc} and the individual overtopping volumes V and their respective marginal distributions $F_{n_{inc}}$ and F_V. Additionally, let's assume a certain threshold u above which, the data belong to the tail. Then the upper tail dependence (λ_U) can be defined as follows (Joe, 2014):

$$\lambda_U = \lim_{u \to 1^-} P(V > F_V^{-1}(u) | n_{inc} > F_{n_{inc}}^{-1}(u)) \tag{5.3}$$

The tail dependence is defined as the probability that, given the first variable is greater than a certain threshold, the second variable is greater than the same threshold, when that is taken as a limit to 1. In a similar manner, the lower tail dependence can be defined. Naturally, since this metric is a conditional probability, it takes values from 0 to 1. However, because of the limit definition, tail dependence cannot be directly inferred from data and an empirical equivalent does not exist (Joe, 2014).

In order to overcome this limitation and draw additional conclusions on the behaviour of the upper tails we fitted theoretical copula functions to the data. A number of different functions were considered and the estimation of the parameters was performed using maximum likelihood. The goodness of fit (GoF) of each candidate was assessed using three metrics, namely the log-Likelihood , the Akaike information criterion (AIC) and the Bayesian information criterion (BIC). However useful, these metrics do not provide direct information about the tail behaviour. For this reason, we calculated the semi-correlations through Monte-Carlo sampling for each candidate copula. The fitted copula function was ultimately decided based on the combination of high GoF metrics and a best match between the theoretical and empirical semi-correlations. For the cases where more than one copula family provided a satisfactory fit, the one with the least number of parameters was chosen. The summary of the fitted copula parameters, their respective semi-correlations and the empirical semi-correlations is presented at Table A.1, Appendix B. Generally, a very good match with the empirical data has been obtained.

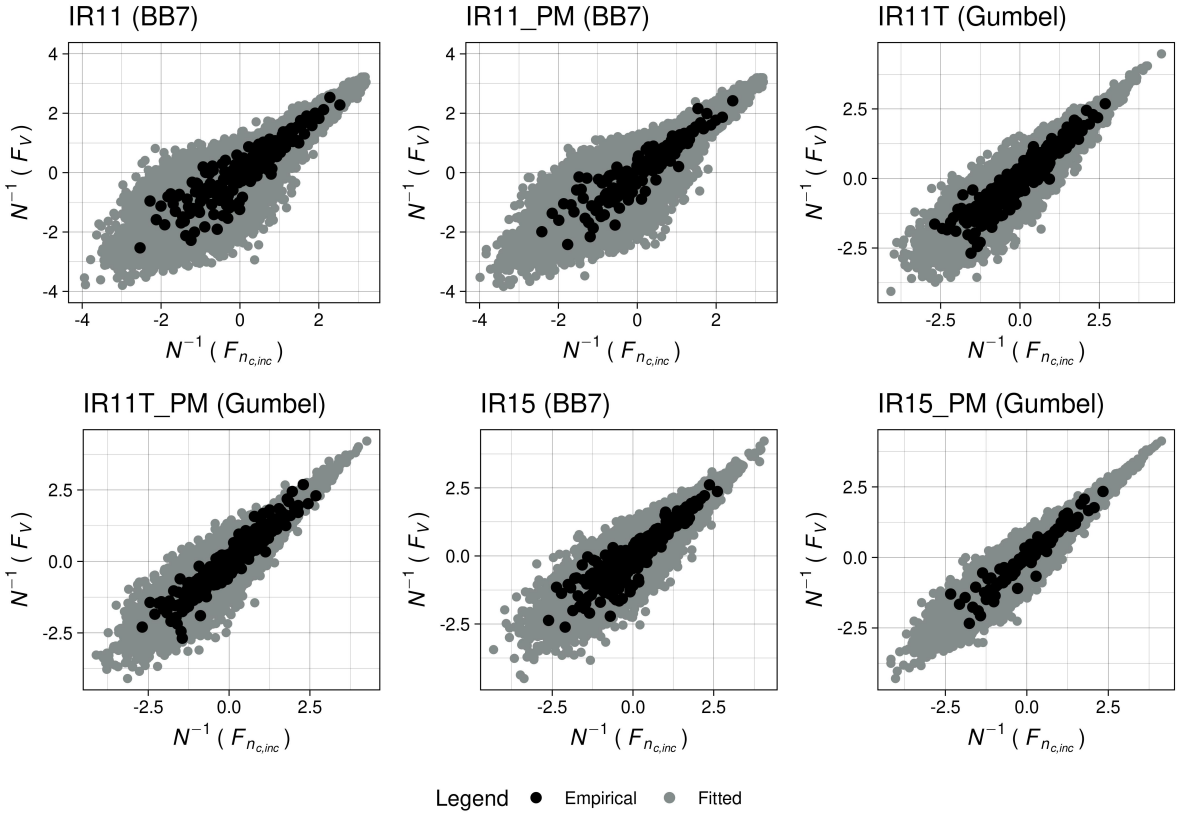

Figure 5.5: Empirical and fitted copula samples between incident wave crest n_{inc} and individual overtopping volumes

Figure 5.5 presents the empirical and fitted copula samples for all cases. It was found that two copula functions can describe the data best, the Gumbel and the BB7. The bivariate Gumbel copula is single parameter function for which only the upper tail dependence is positive. The BB7 is a two-parameter copula family was introduced by Joe and Hu (1996). For this copula, both upper and lower tail dependence can be positive. This is probably the most notable difference between the two. However, any physical implications from the presence of lower dependence are not discussed herein, since the focus of this study is on the larger events. It should also be noted that the extreme value limits of the upper tail of the BB7 copula converge to the Gumbel copula (Joe, 2014). The cumulative distribution functions (CDF) of both copulas, as well as those who will be mentioned in the subsequent sections, are given in Appendix B.

Having fitted the data to the theoretical copulas, the upper tail dependence for each case can be calculated. These are presented in Table 5.4. It appears that, for all cases, λ_U is very similar. Specifically, it ranges from 0.83 to 0.88 with an average of 0.85, despite the different copulas. This might be explained by the fact that the upper tails of the two copulas converge, as it was previously mentioned. This result effectively means that, given an extreme incident wave crest, there is approximately 85% probability that the percentile of the resulting overtopping volume will be higher than that of the crest.

Table 5.4: Upper tail dependence coefficients derived from the fitted wave crest - overtopping volume copulas

Scenario	λ_U
IR11	0.85
IR11_PM	0.85
IR11T	0.83
IR11T_PM	0.84
IR15	0.85
IR15_PM	0.88

Finally, for completeness, we provide a comparison between the wave crest/overtopping volume and wave height/overtopping volume copulas. For brevity, only a single case, IR11T is presented in the main text. Following the same procedure as previously, the best fit copula for the wave height/overtopping volume pair was determined to be the BB8 (Joe, 1993). The empirical and fitted copulas are presented in Figure 5.6. It is observed that the shape of the wave crest/overtopping volume copula is much narrower than the wave height/overtopping volume copula, which is expected, since the rank correlation of the former pair of variables is higher (0.94) than the one of the latter pair (0.7). However, the key difference lies in the fact that the upper tail dependence of the fitted BB8 copula is equal to zero. In order to exemplify this difference, we choose a threshold equal to $u = 99.86\%$ (which is equivalent to $z = 3$ in the standard normal space). This is denoted by black dashed lines in Figure 5.6. Then, we mark the events where both the wave crest and the corresponding volume are above u with red, and the events where the wave crest is above the threshold but the corresponding volume is below, in orange. In the case of the wave crest/volume copula (subplot a, Figure 5.6) , for 82% of the events which have a crest value above u, the volume is also above the same threshold (red points in Figure 5.6). In the case of the wave height/volume copula (subplot b, Figure 5.6) the percentage of events where both the wave height and the overtopping volume are above u (red points in Figure 5.6) is equal to 0.08% of the total events where the wave height is above the same threshold. Those two values can be loosely translated as the empirical "tail" dependence of the copulas above the given threshold. In practice, they help to illustrate that, most likely, a large wave will result in an overtopping volume with lower probability of occurrence than that of the wave height.

The same procedure for fitting copulas between the wave height and overtopping volume pairs, was repeated for all other numerical cases. The BB8 copula was found to be the best fit for all cases (see Appendix A.6). Moreover, based on the fitting of the BB8 copulas, it was determined that in every case the tail dependence of the wave height/volume pair was equal to zero.

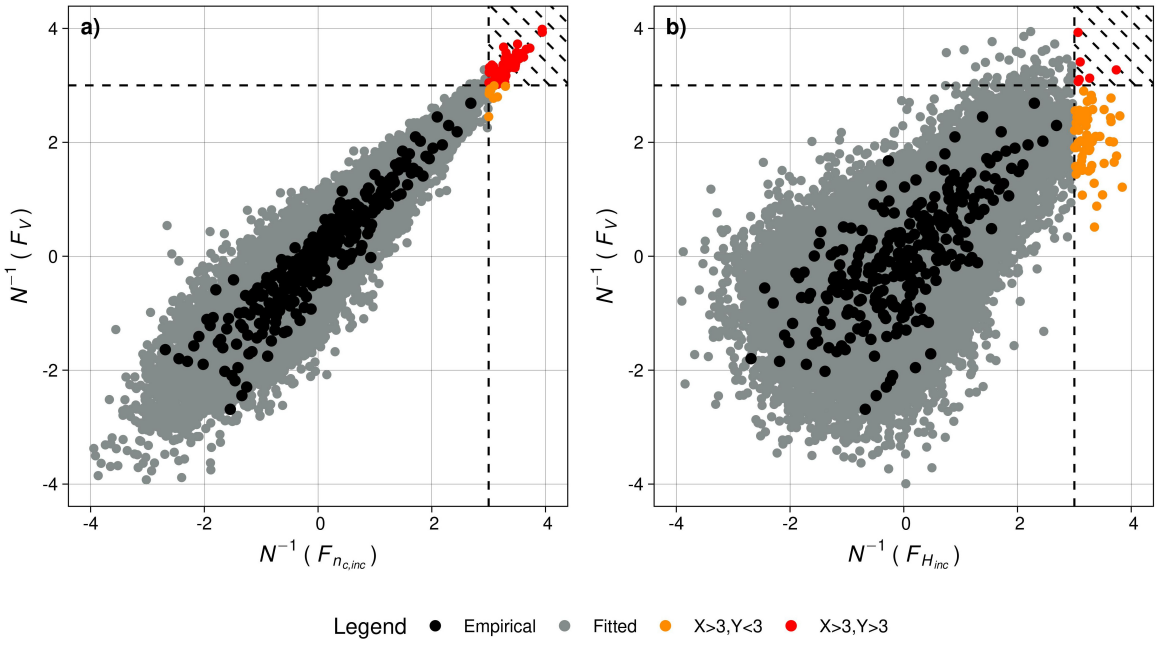

Figure 5.6: Empirical and fitted copula samples between the wave crest/overtopping volumes (a) and the wave height/overtopping volume (b) for case IR011_T. The red points denote volumes above the 99.86% threshold while the orange points denote volumes below the same threshold. The threshold is denoted by the black dashed lines.

6

Effect of wave group

In the previous section we investigated the dependencies of the individual overtopping volumes with the incident waves and the highest correlation was found to be with the incident wave crests. However, overtopping volumes could be additionally influenced by wave groups. For example, there may be set-up generated at the toe of the breakwater due to a very long incident wave group. In this section we will investigate the dependencies between the wave group and the overtopping volumes using three variables, the wave group period, the total wave group energy and the wave group energy divided by the group period.

The definition of a wave group from a surface elevation record is not a straightforward task and different methods exist. Perhaps the most commonly used is the envelope method (Adcock et al., 2015; Haller & Dalrymple, 1995; Sobey & Liang, 1987). This method was introduced by Longuet-Higgins (1984) and defines a wave group as an excursion of the wave envelope above a predefined threshold. However, as discussed in the work of W. Huang and Dong (2021), this method is very sensitive to the presence of high frequency components (e.g. 2nd order components) and can lead to wave groups which contain only a single wave. In the same work the authors compare two additional methods to define wave groups from a surface elevation record, the smoothed instantaneous wave energy history (SIWEH, Funke and Mansard, 1979) and the wavelet transform (Torrence & Compo, 1998). Their results show that the two methods have similar performance in identifying wave groups. Thus in this study we chose to employ SIWEH over the wavelet transform due to it's simplicity. SIWEH was introduced by Funke and Mansard (1979). They defined the instantaneous wave energy process ($E_s(t)$) as:

$$E_s(t) = \frac{1}{T_p}\int_{-\infty}^{\infty} n^2(t+\xi)Q(\xi)d\xi \tag{6.1}$$

where n is the water surface elevation, T_p is peak period and Q is the Bartlett window function given by the following equation:

$$Q(\xi) = \begin{cases} 1 - \frac{|\xi|}{T_p}, & -T_p \leq \xi < T_p \\ 0, & \text{otherwise} \end{cases} \tag{6.2}$$

Once the instantaneous wave energy timeseries are calculated, a wave group can be defined as the exceedance of $E_s(t)$ over a certain threshold. According to W. Huang and Dong (2021), the threshold $\tilde{E}$ should be set to $\tilde{E} \approx 0.08H_s^2$. This value is adopted herein. An example of the wave group identification for case IR011_T is given in Figure 6.1. In this figure, the wave groups are marked with grey shaded areas and numbered with Roman numerals.

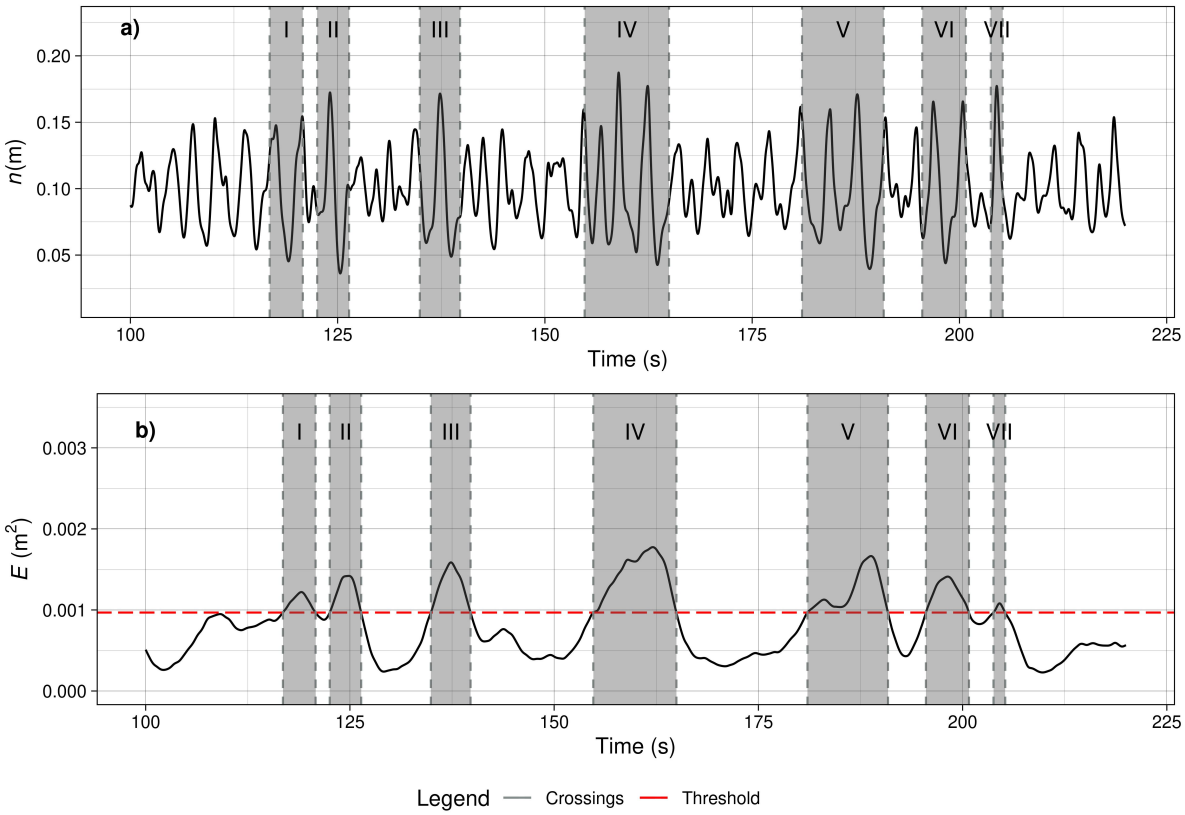

Figure 6.1: Example of wave group definition using SIWEH for case IR011_T. a) shows the free surface record and the threshold crossing. b) shows the instantaneous wave energy $E_s(t)$, the energy threshold and the threshold crossings. The grey shaded regions denote the wave groups and are numbered by Roman numerals.

By applying the SIWEH method we identified the wave groups for every scenario. For this calculation, the incident wave field at the toe of the breakwater ($x = 33.3m.$), derived from OceanWave3D, is used. Once the wave groups are identified, each group is associated with the corresponding overtopping events. These are simply defined as events which result from a wave crest that belongs to a given group. For the cases where more than one overtopping events belong in the same wave group, the one with the maximum volume is taken as the representative event. Following this methodology, we produce a set of wave groups/overtopping volumes for each case. The number of overtopping wave groups (N_{og}) is given in Table 6.1. It is noted that the wave group sample is smaller than the individual wave sample for every case. For example, scenario IR15_PM 103 individual overtopping waves are simulated but the number of overtopping wave groups is 58. These reduced samples will lead to increased uncertainty in the calculation of the subsequent statistics.

Table 6.1: Number of overtopping wave groups

Scenario	N_{og}
IR11	93
IR11_PM	76
IR11T	110
IR11T_PM	114
IR15	95
IR15_PM	58

6.1. Wave group period

The first variable to use for the quantification of the effect of the wave groups in the individual overtopping is the wave group period. The wave group period T_g is defined as the time between two consecutive

threshold crossings of the instantaneous wave energy. Graphically, this is represented by the width of the grey shaded regions in Figure 6.1. As supplement to the wave group identification, Table A.2 briefly presents some wave group period statistics.

As a first step of the analysis, the Spearman rank correlation between the wave group period and the overtopping volumes is calculated for all cases and it is found to be between 0.42 and 0.67. These results indicate that the length of the wave group has an non-negligible influence in the individual overtopping volumes.

Table 6.2: Spearman Rank Correlation of individual overtopping volumes and wave group periods T_g

Scenario/Spearman Rank	T_g
IR11	0.63
IR11_PM	0.46
IR11T	0.67
IR11T_PM	0.63
IR15	0.42
IR15_PM	0.50

To fully explore the dependence structure between the two variables, we employ once more the copula methodology. For every case we fit theoretical copula function between the wave group period and associated overtopping volumes,by following the same procedure as demonstrated previously. It is found that the Frank copula is the best fit for all cases, except IR15 for which the Gaussian copula fitted better. Scatter plots of the empirical and fitted copula samples are presented in Figure 6.2. The summary of the fitted copula parameters, their respective semi-correlations and the empirical semi-correlations is presented at Table A.3, Appendix B. It is observed that in contrary to the wave crest, the dependence structure between wave group periods and overtopping volumes is fairly symmetric.

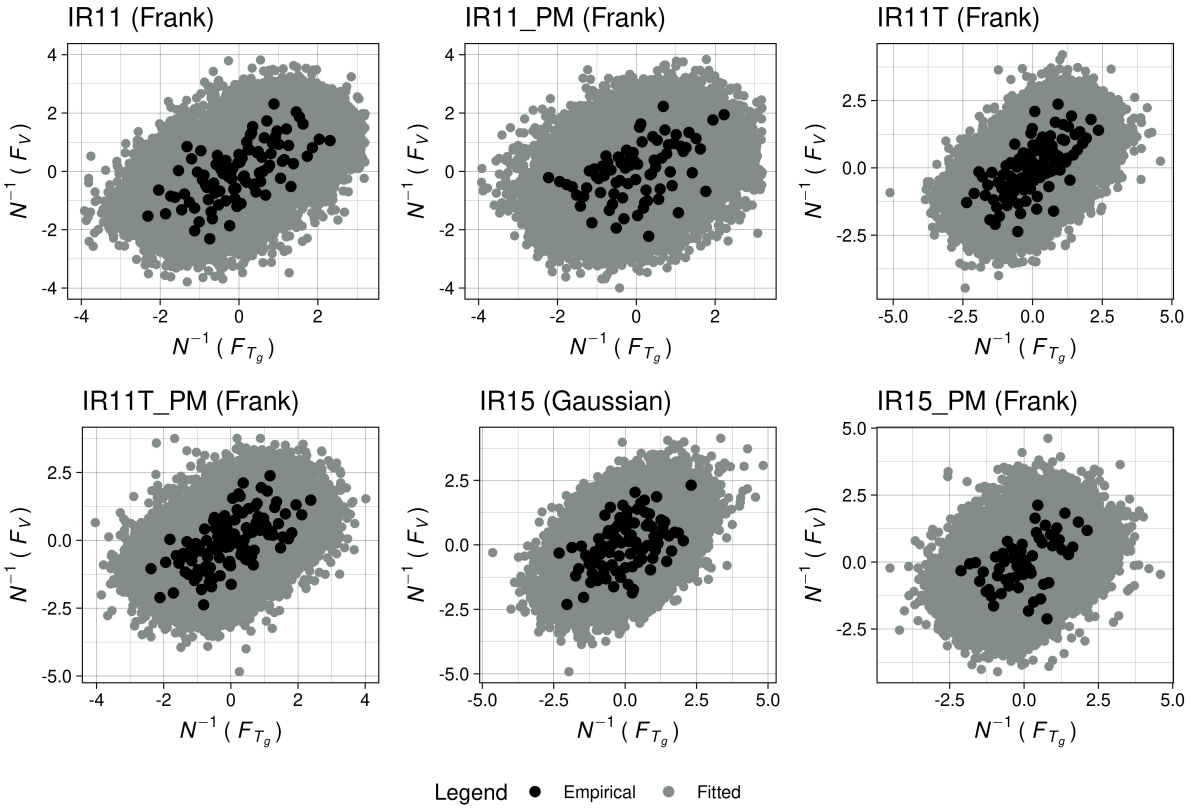

Figure 6.2: Empirical and fitted copula samples between incident wave crest n_{inc} and individual overtopping volumes

Furthermore, the tail dependence of the Frank and Gaussian copulas is zero. In practical terms, this means that high wave group periods will not necessarily result in equally high overtopping volumes. Again, this is contrary to the strong upper tail dependence that was found between the wave crest and overtopping volumes. However, the high rank correlations indicate that the wave groups do have a positive influence in overtopping and they should be taken into account.

6.2. Wave group energy

Having calculated the instantaneous wave energy through SIWEH, we can also calculate the total energy within each group, denoted by E_g, by integrating $E_s(t)$ over the group period. In this way we can assess if the most energetic wave groups lead to the highest overtopping volumes. However, E_g may not necessarily be the best descriptor of a highly "energetic" wave group because it depends on the period of the group. Thus, a longer group may lead to higher total energy but contain moderate amplitude waves. To account for that, we define the wave group energy density as the fraction between the total group energy and the group period, i.e. $E_{gd} = E_g/T_g$. As before, we calculate the Spearman rank correlation between the two pairs of variables. Additionally, we calculate the semi-correlations as defined by equation 5.2.

Table 6.3: Spearman rank correlations and semi-correlations of pairs between wave group energy (E_g) and energy density E_{gd} with overtopping volumes

Scenarios	Spearman Rank		ρ_N^+		ρ_N^-	
	E_g	E_{gd}	E_g	E_{gd}	E_g	E_{gd}
IR11	0.68	0.72	0.44	0.77	0.31	0.33
IR11_PM	0.52	0.64	0.44	0.54	-0.27	-0.11
IR11T	0.73	0.83	0.39	0.70	0.09	0.36
IR11T_PM	0.71	0.80	0.27	0.61	0.25	0.32
IR15	0.47	0.62	0.01	0.37	-0.07	0.06
IR15_PM	0.51	0.55	0.20	0.59	-0.11	-0.10

Table 6.3 presents the rank and semi-correlation results. It is observed that consistently the wave group energy density produces higher rank correlations than the wave group energy. More importantly, E_{gd} demonstrates notably higher upper semi-correlations than the ones obtained with E_g, especially for cases IR15 and IR15_PM. This means that larger overtopping events have a high correlations with the wave group energy density. Conversely, the lower semi-correlations appear weaker and even negative in certain cases. It should be noted that the negative values have no physical interpretation and it can be shown through bootstrapping (not presented here) that this is the result of statistical uncertainty due to the small sample size. For example, IR11_PM includes only 24 events in the lower quadrant.

Again, to investigate this dependence we fit theoretical copulas to the data and plot the comparison between theoretical and empirical copulas in Figure 6.3. From this analysis we find that in the majority of the cases the Gumbel copula is best fit, with the exception of two cases. For scenario IR15_PM the BB7 copula fits best to the data. As discussed earlier, the extreme value limits of the tail of this copula converge to the Gumbel copula. For scenario IR11_PM the best fit copula is the BB8. This copula does not have upper tail dependence, which is contrary to Gumbel and BB7. From the fitted copulas, the upper tail dependencies of equation 5.3 are calculated and presented in Table 6.4. From the cases that do exhibit upper tail dependence, this varies between 0.48 to 0.71 with an average value of 0.62. This value is lower than the one obtained from the incident wave crest - overtopping volume analysis, which was equal to 0.85.

Table 6.4: Upper tail dependence coefficients derived from the fitted wave group energy density - overtopping volume copulas

Scenario	λ_u
IR11	0.63
IR11_PM	0.00
IR11T	0.71
IR11T_PM	0.66
IR15	0.48
IR15_PM	0.60

However, it demonstrates that when an ”energy dense” wave group is incident, it will most likely result in high overtopping volumes. The exception to the above, is case IR11_PM for which no upper tail dependence is found. This can be attributed to fitting uncertainty, since this case has the second lowest sample size with 76 observations. The summary of the fitted copula parameters, their respective semi-correlations and the empirical semi-correlations is presented at Table A.4, Appendix B.

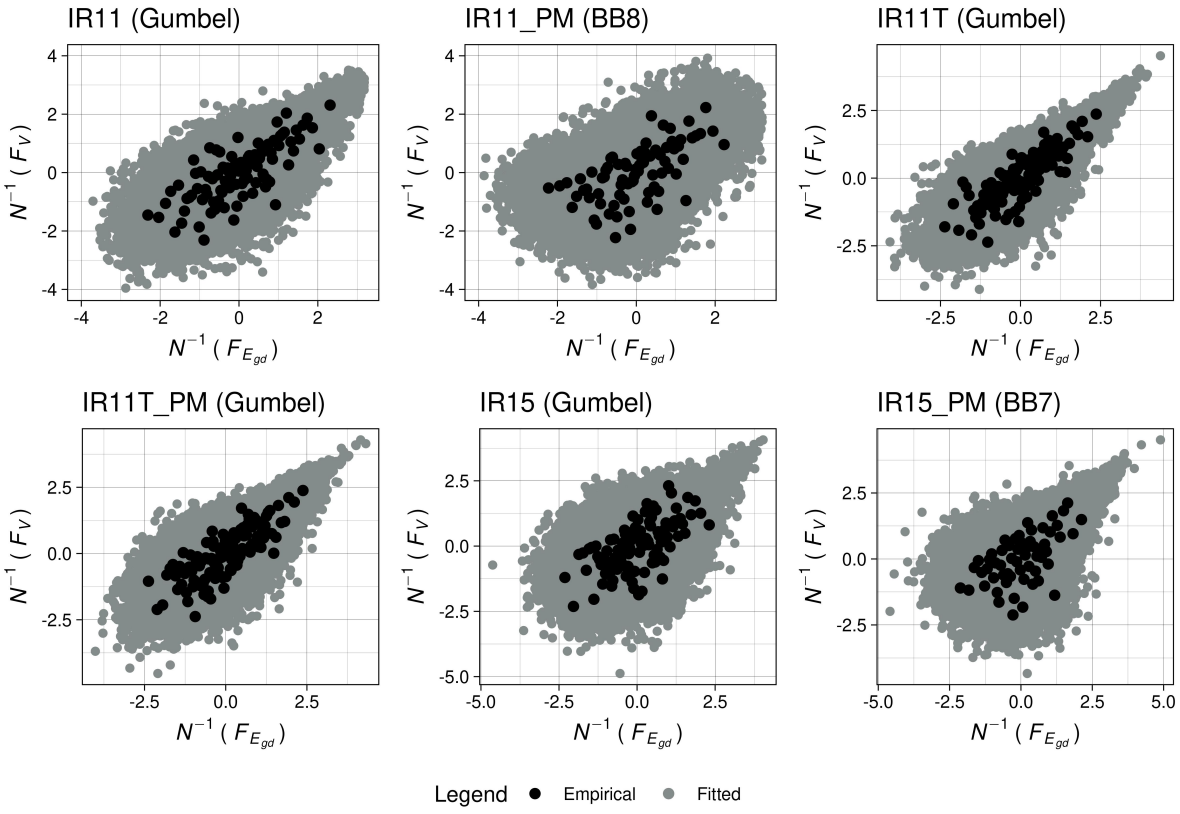

Figure 6.3: Empirical and fitted copula samples between incident wave group energy density E_{gd} and individual overtopping volumes

7

Discussion

As shown earlier in Figure 5.5, the incident crest levels and overtopping volumes exhibit strong upper tail dependence. This means that there is a high probability, 85% on average in our results, that the percentile of the resulting overtopping volume will be higher than the one of the corresponding wave crest. Thus, if the probability of the incident wave crest is known, a range of the overtopping probability can be estimated with a given certainty. This finding may be able to support a methodology for simulating extreme overtopping volumes using a reduced number of waves. Such a methodology could be comprised of the following steps. Firstly, the incident wave field would be simulated for the entire length of the domain. Then the waves with the largest wave crest elevations and their corresponding wave groups, at the toe of the breakwater, would be identified. Subsequently, the incident wave groups would be used to force a wave-structure interaction model (e.g. OpenFOAM, physical model) and the overtopping volumes would be calculated. Finally, the range of the probability of the resulting overtopping volume from a given wave crest would be indirectly estimated with the help of the tail dependence definition.

Here, an important distinction must be made. So far, the probabilities of the wave crests that have been presented refer to events where the particular wave overtopped. In other words, these probabilities (e.g. the exceedance probabilities of Equation 5.3) are conditional to the volume being positive. Mathematically, this is defined as $P(n_{c,inc} > n|V(n_{c,inc}) > 0)$. However, from the simulation of the incident wave field, only the marginal wave crest probability $P(n_{c,inc} < n)$ can be estimated. Therefore, in order use the incident wave simulation to estimate the probability range of an overtopping volume, an additional relationship is required to estimate the conditional probability $P(n_{c,inc} > n|V(n_{c,inc}) > 0)$ from the marginal $P(n_{c,inc} < n)$. To tackle this, overtopping can be considered as a threshold process of the wave crest. In other words $P(V > 0) = P(n_{c,inc} > n_u)$. n_u is an incident wave crest level (i.e. a threshold) above which it is assumed that all waves overtop. Subsequently is follows that, the distribution of the threshold exceedances is given by (Coles, 2001):

$$P(n_{c,inc} > n|n_{c,inc} > n_u) = \frac{P(n_{c,inc} > n)}{P(n_{c,inc} > n_u)} \tag{7.1}$$

The above formulation has the benefit that the terms of the right hand side fraction can be known or estimated a-priori. Specifically, $P(n_{c,inc} > n_u) = P(V > 0)$ is the probability of overtopping P_{OW} and it can be estimated using EurOtop's empirical relationship, as previously demonstrated. The marginal wave crest probability of exceedance $P(n_{c,inc} > n) = 1 - P(n_{c,inc} < n)$ can be directly estimated from analysing the simulated incident wave crest record. Based on the above, $P(n_{c,inc} > n|V(n_{c,inc}) > 0)$ can be estimated. Then according to the calculated tail dependence, there is a 0.85 probability that $V > F_v^{-1}(P(n_{c,inc} > n|V(n_{c,inc}) > 0))$.

Another remark can be made about the uniformity of the derived tail dependencies. As mentioned earlier their values range from 0.83 to 0.88. Additionally, despite the different copula functions fitted to the data, Gumbel and BB7, the tail of the latter converges to a Gumbel shape. These findings may indicate some general trend regarding the behaviour of the joint tail of wave crests and overtopping volumes and should be further investigated. If shown by subsequent studies, that indeed there is con-

sistency across different cases, this could further motivate the use of the tail dependence in estimating the probability of overtopping through the probability of the incident wave crests.

Moreover, we should also note that in the current study, the differences between different boundary conditions were not discussed in detail. This is partly due to the fact that across all cases the wave crest dependencies were dominant. Additionally, due to time limitations, only two different peak periods and relative freeboards were examined, which do not provide a large enough set to draw conclusions about potential differences between them. This is a current limitation of the study, which should be addressed in future research. Perhaps a larger group of simulations can be defined based on the spectral shape. In our analysis, each set of boundary conditions was run with a JONSWAP and P-M spectra. However, no discernible differences where identified between the two. This is in line with the results of Laface et al. (2018), in which they showed through a second order theoretical model, that the influence of the spectral shape in the distribution of the wave crest at the toe of the breakwater is negligible.

Finally, it should be stressed that the above results, refer only to non-breaking waves and vertical structures. In porous structures there could be additional mechanisms that influence overtopping. For example, preceding waves may saturate the core layers and thus increase overtopping. This could be the mechanism which Gunbak and Bruun (1979) observed in the physical experiments of rubble mound breakwaters. Those aspects should be further investigated.

8

Conclusions

In the present work we investigated the statistical relationships of individual overtopping volumes with wave characteristics on vertical wall breakwaters under non-breaking waves. For this purpose, a coupled OceanWave3D/OpenFOAM model was validated against experimental data and it was subsequently used to generate a data set of waves and individual overtopping volumes. During the validation procedure, care was taken in the selection of the interface method. After evaluation, it was found that isoAdvector was superior to MULES in terms of accuracy and sensitivity to the choice of the CFL number. In total, 6 wave cases were examined, with varying wave conditions and relative freeboard. The numerical results were compared against EurOtop empirical formulas for the mean overtopping discharge, maximum overtopping volume, percentage of overtopping waves and distribution of individual overtopping volumes and good agreement was found between the two.

The investigation of overtopping dependencies was focused on different parameters of the incident wave field. For all cases it was observed that above a certain incident wave height threshold, which was approximately 80% of the recorded maximum incident wave height, similar wave heights resulted in significantly different individual overtopping volumes. On the contrary, the incident wave crest level showed almost a one to one relationship with the volumes. Furthermore, the dependence structure was examined by employing copulas to study the joint distribution, without the effects of the marginals. It was found that the best fit copulas to the data were the Gumbel and the BB7. By utilising the theoretical copula functions, it was found that the incident wave crest and individual overtopping volumes show strong tail dependence. This ranged from 0.83 to 0.88, with an average of 0.85. The same procedure was repeated for the incident wave height and no upper tail dependence was found.

Additionally, the correlations with other variables were examined, namely the wave period, the wave trough level and the wave steepness. All of the above showed very weak correlations with overtopping, with the exception of the steepness, which was found to be approximately 0.50. However, this was not investigated further, since the correlation of the crests was dominating all cases.

Finally, the influence of the wave group in the overtopping volumes, by means of the wave group period, the wave group energy and the wave group energy density, was assessed and found to be important. Specifically, the Spearman rank correlation between the wave group periods and the overtopping volumes ranged between 0.42 and 0.67. Again, copulas were used to examine the dependence structure between the two variables. It was found that the Frank and the Gaussian copulas were the best fits for the data. Based on those copula functions, no upper tail dependence between the wave group period and the overtopping volumes was found. Moreover, to examine the dependencies of the wave group energy two variables were used, the total wave group energy and the wave group energy density, in order to take into account the effect of the wave group period. The analysis showed that the latter variable demonstrates higher rank correlation and upper semi-correlations with the individual overtopping volumes than the former. The rank correlations ranged between 0.55 and 0.83. Additionally, through the fitting of theoretical copulas to the data it was demonstrated that the wave group energy density exhibits non-negligible upper tail dependence with the overtopping volumes, with an average value of 0.62, with the exception of one case.

Overall, our results provide evidence that in the case of vertical wall breakwaters under non-breaking waves, the incident waves with the highest crest elevations will produce the most severe overtopping

events. Moreover, our analysis shows that incident wave groups with high energy density, defined as the fraction between the wave group energy and the group period, are also strongly related to severe overtopping events.

A

Supplementary material to the analysis

A.1. Water surface elevation plots during selected overtopping events

In the present appendix we showcase the qualitative differences between cases with equal or almost equal wave height but vastly different overtopping volumes.

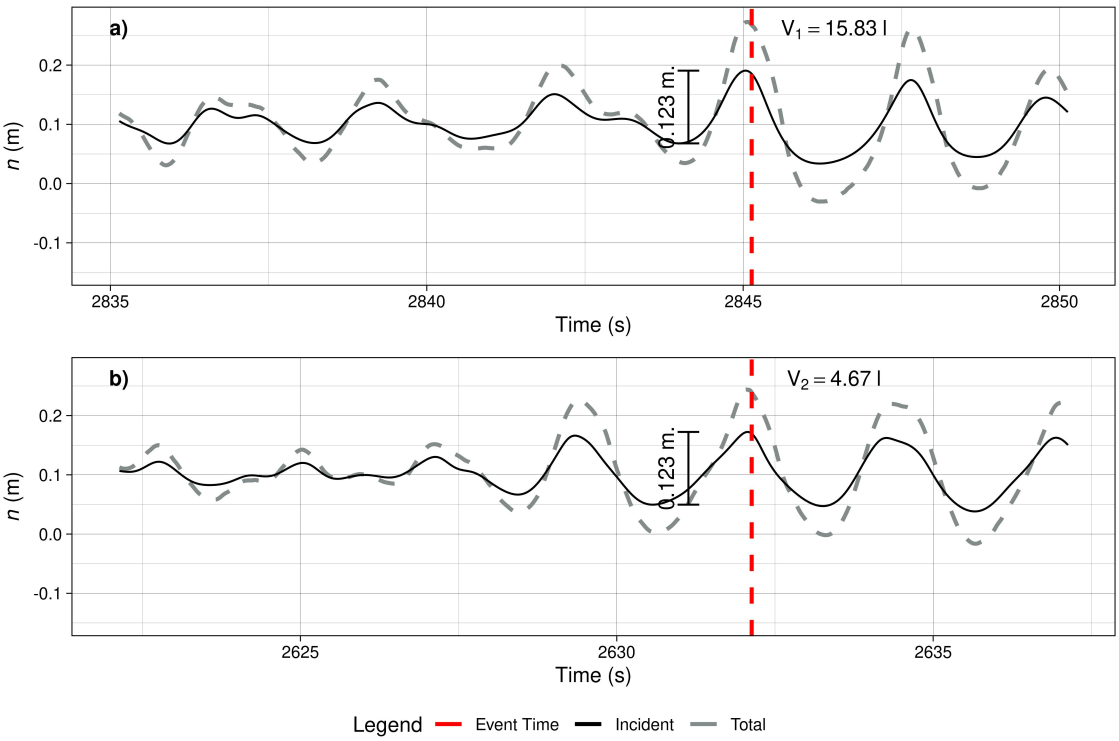

Figure A.1: Incident and total water surface elevation for two realisations of an incident wave $H_{inc}/H_{inc,max} \approx \%80$ with different overtopping volumes. Case IR11

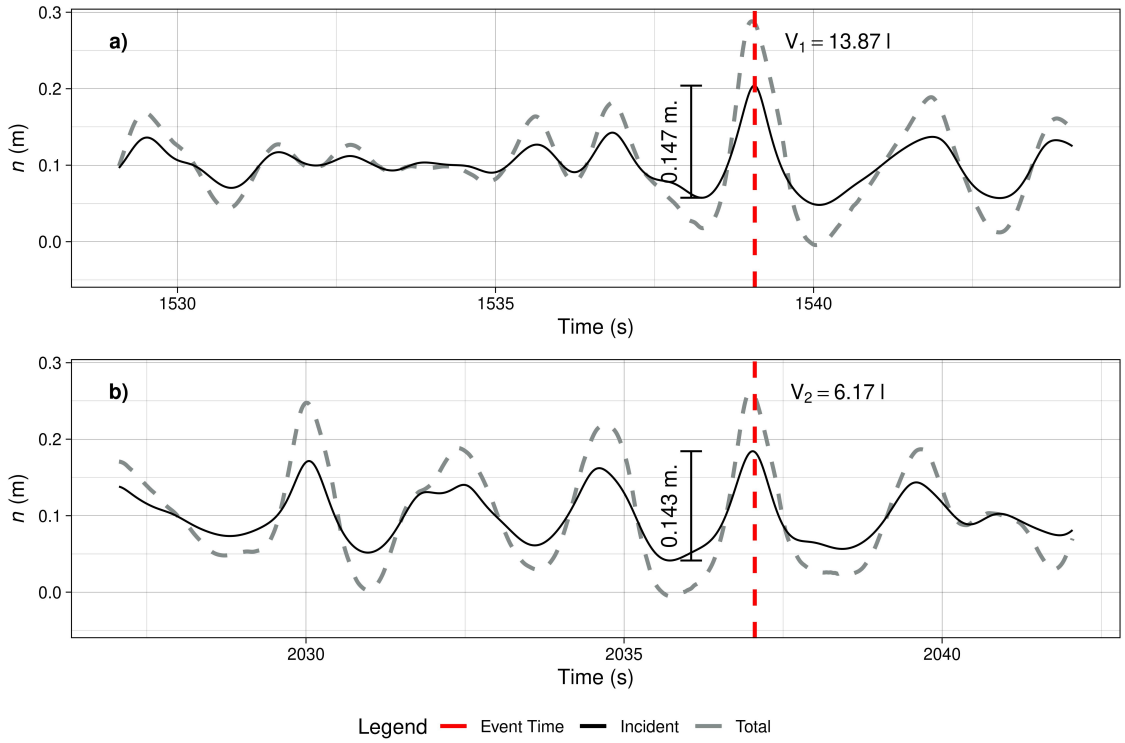

Figure A.2: Incident and total water surface elevation for two realisations of an incident wave $H_{inc}/H_{inc,max} \approx \%80$ with different overtopping volumes. Case IR11_PM

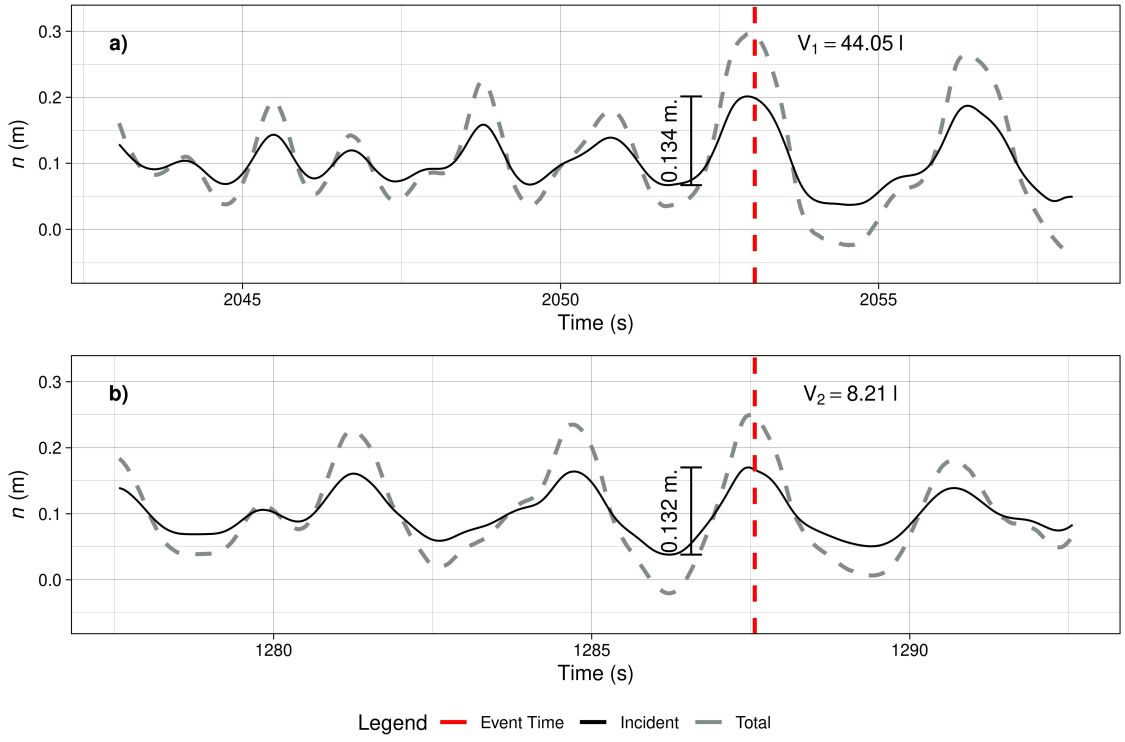

Figure A.3: Incident and total water surface elevation for two realisations of an incident wave $H_{inc}/H_{inc,max} \approx \%80$ with different overtopping volumes. Case IR11T_PM

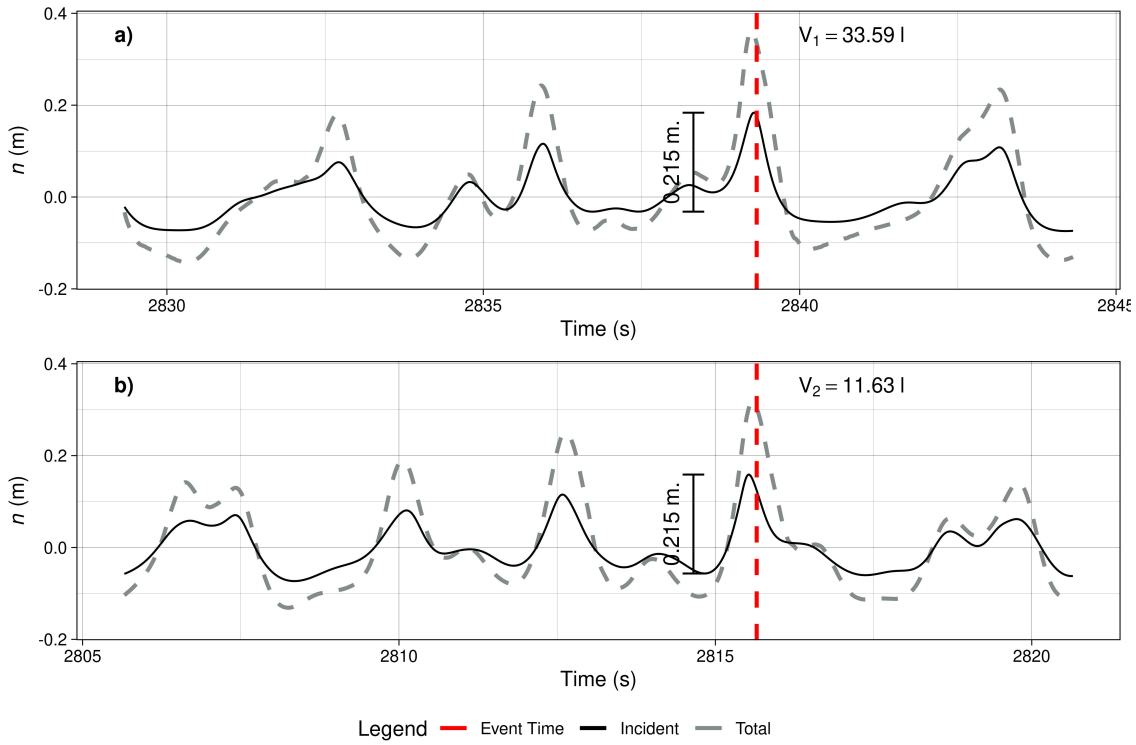

Figure A.4: Incident and total water surface elevation for two realisations of an incident wave $H_{inc}/H_{inc,max} \approx \%80$ with different overtopping volumes. Case IR15

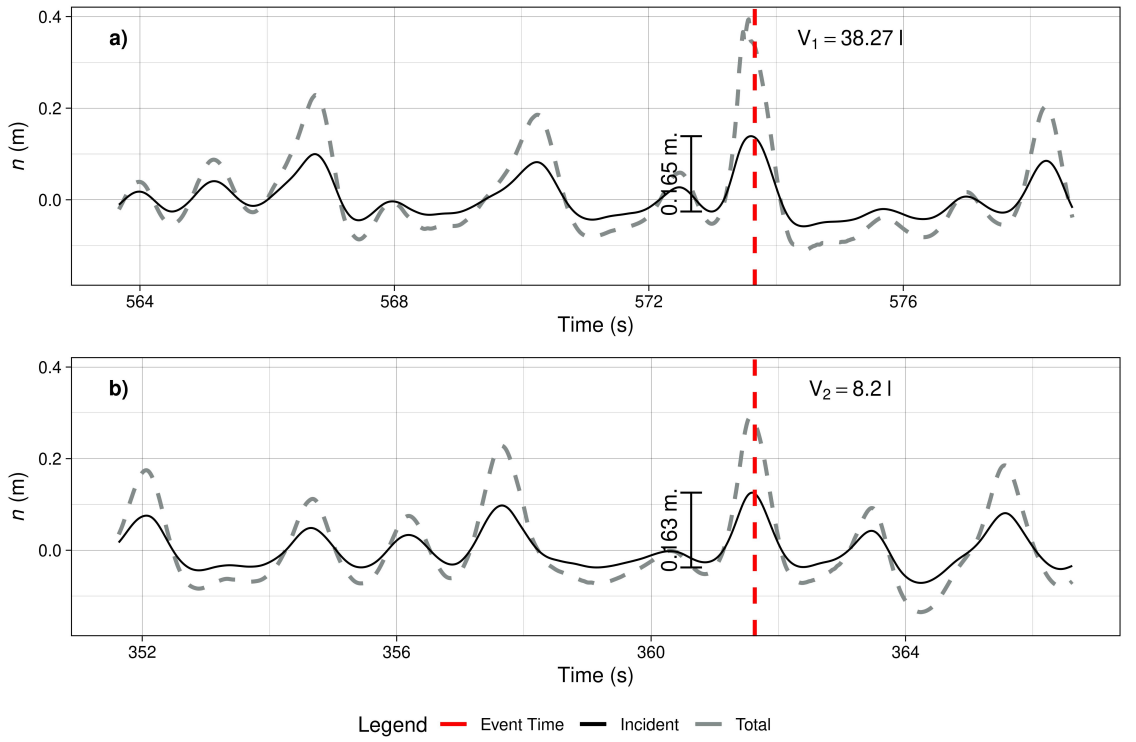

Figure A.5: Incident and total water surface elevation for two realisations of an incident wave $H_{inc}/H_{inc,max} \approx \%80$ with different overtopping volumes. Case IR15_PM

A.2. Scatter plots of incident wave height and wave crest to individual overtopping volumes normalised by their average value

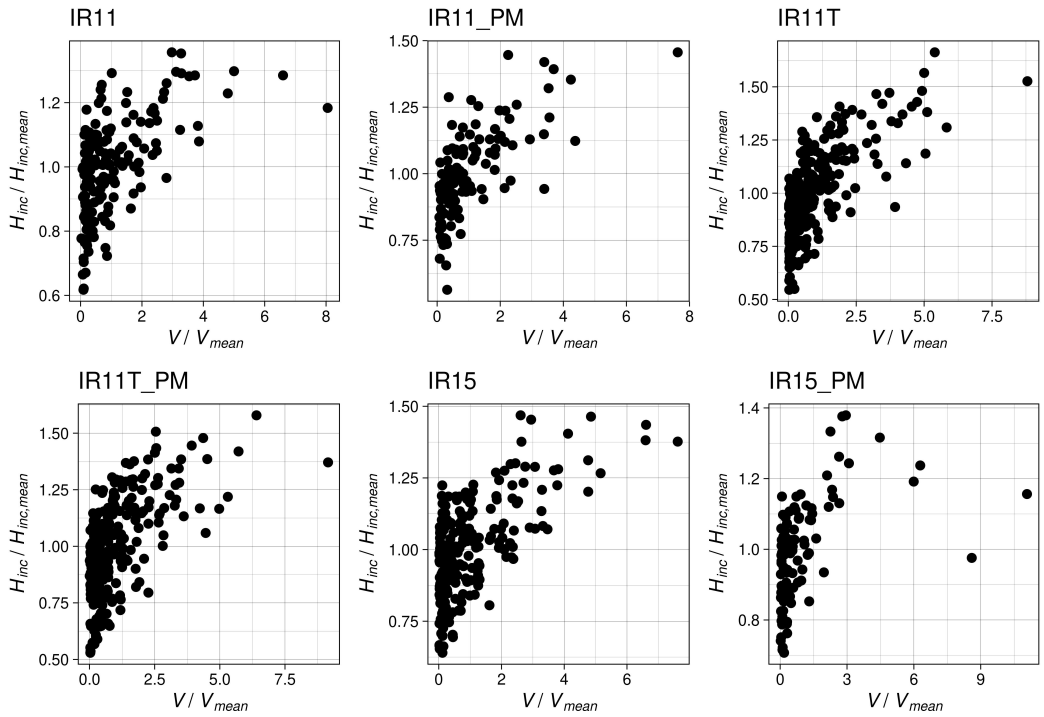

Figure A.6: Scatter plot between incident wave height H_{inc} and individual overtopping volumes V normalised by their average values

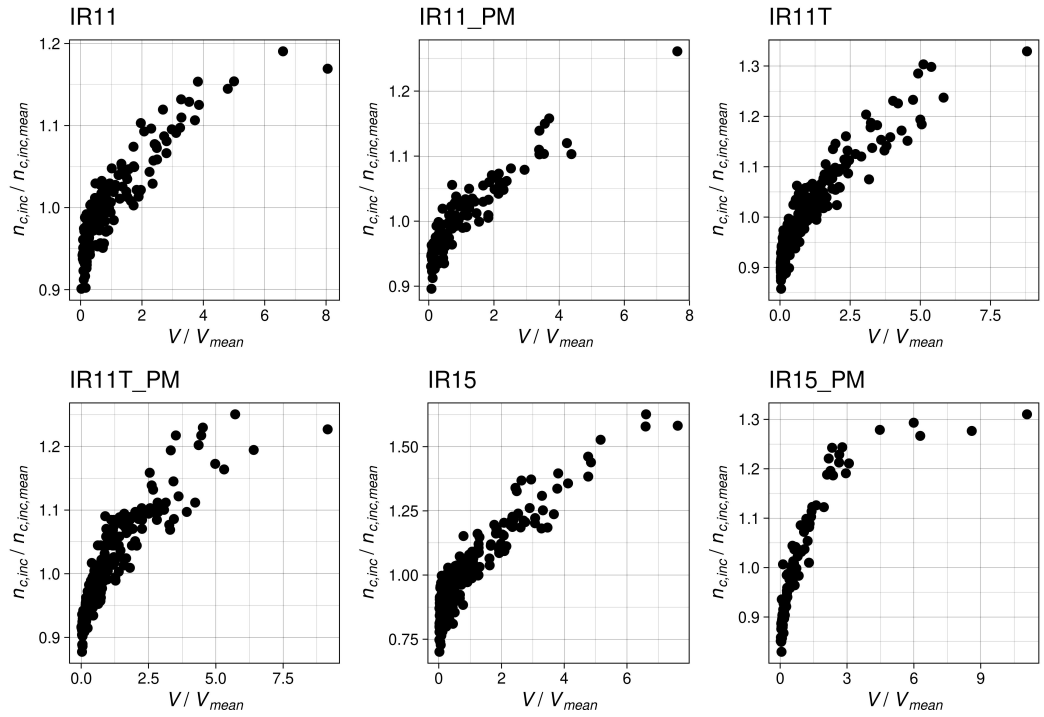

Figure A.7: Scatter plot between incident wave crests $n_{c,inc}$ and individual overtopping volumes V normalised by their average values

A.3. Scatter plots between wave crest of the total signal and individual overtopping volumes

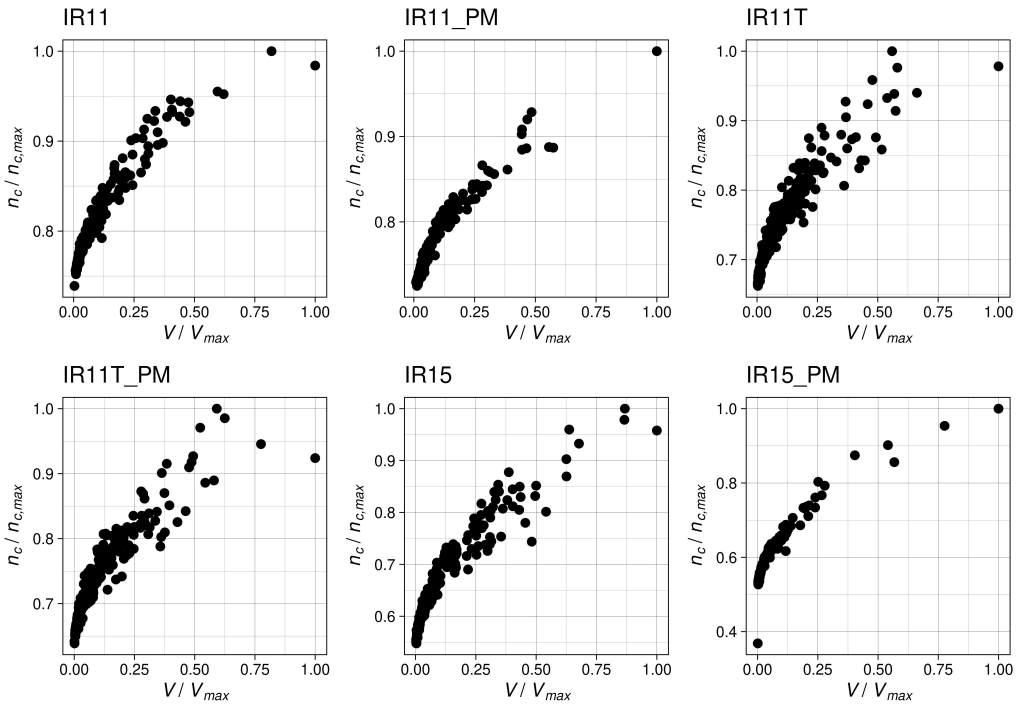

Figure A.8: Scatter plot between total (incident + reflected) wave crest n and individual overtopping volumes V normalise by their maximum values

A.4. Examples of different fitted copulas for case IR11T

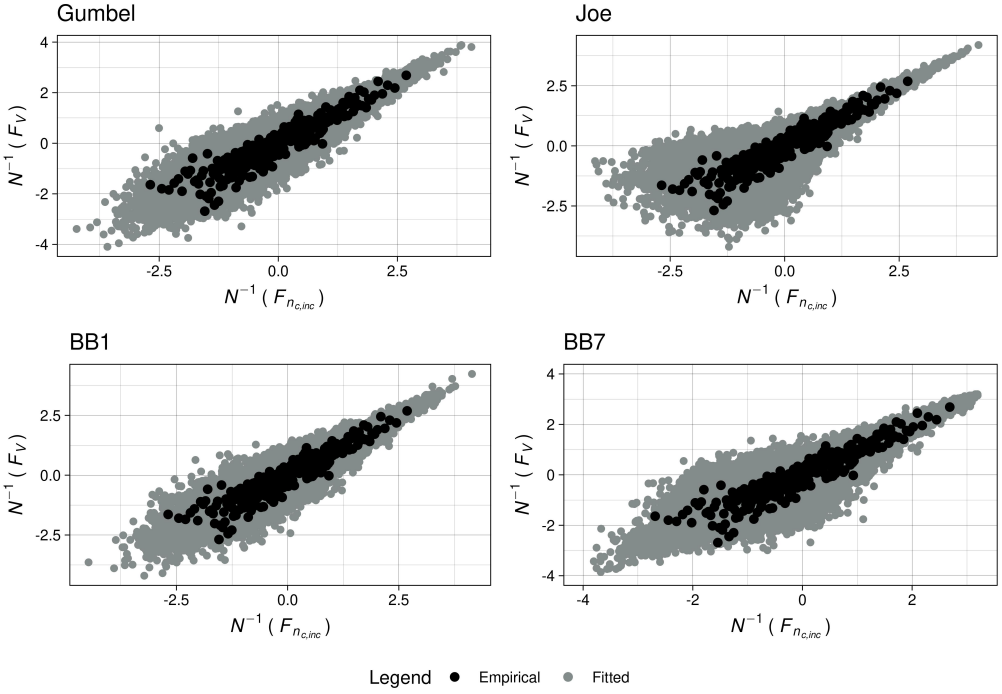

Figure A.9: Different copulas fitted for case IR11T

A.5. Parameters of the fitted incident wave crest - overtopping volume copulas

Table A.1: Summary of semi-correlations and parameters of the fitted wave crest - overtopping volume copulas. Note that the subscript E in this table, denotes the empirical semi-correlations which were calculated from the numerical data.

Scenario	Copula	Par1	Par2	λ_U	ρ_N^+	ρ_N^-	$\rho_{N,E}^+$	$\rho_{N,E}^-$
IR11	BB7	4.94	0.62	0.85	0.91	0.56	0.89	0.52
IR11_PM	BB7	5.00	0.78	0.85	0.91	0.6	0.88	0.58
IR11T	Gumbel	4.37	0.00	0.83	0.91	0.76	0.9	0.7
IR11T_PM	Gumbel	4.72	0.00	0.84	0.92	0.79	0.88	0.83
IR15	BB7	5.00	0.66	0.85	0.91	0.57	0.93	0.52
IR15_PM	Gumbel	6.12	0.00	0.88	0.95	0.86	0.95	0.81

A.6. Empirical and fitted copulas between incident wave height and overtopping volumes

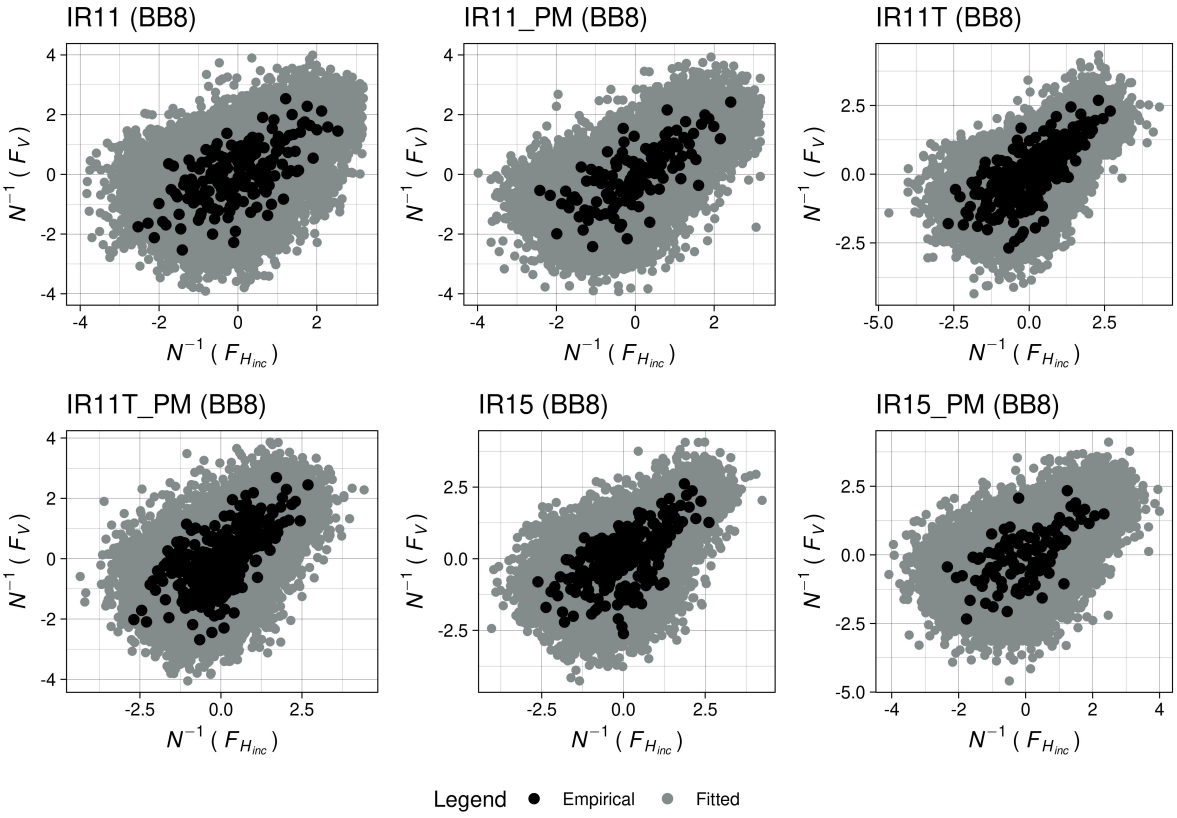

Figure A.10: Empirical and fitted (BB8) copulas between incident wave height H_{inc} and individual overtopping volumes

A.7. Wave group period statistics

Table A.2: Wave group period (T_g) statistics for all simulated cases.

Scenario	μ_{T_g}	σ_{T_g}
IR11	4.40	3.21
IR11_PM	3.18	2.00
IR11T	7.00	5.22
IR11T_PM	5.77	4.01
IR15	9.71	8.14
IR15_PM	4.99	4.03

A.8. Parameters of the fitted incident wave group period - overtopping volume copulas

Table A.3: Summary of semi-correlations and parameters of the fitted wave group period - overtopping volume copulas. Note that the subscript E in this table, denotes the empirical semi-correlations which were calculated from the numerical data.

Scenario	Copula	Par1	Par2	λ_U	ρ_N^+	ρ_N^-	$\rho_{N,E}^+$	$\rho_{N,E}^-$
IR11	Frank	4.80	0	0	0.26	0.25	0.22	0.23
IR11_PM	Frank	3.00	0	0	0.15	0.16	0.3	-0.21
IR11T	Frank	5.22	0	0	0.3	0.29	0.27	0.1
IR11T_PM	Frank	4.52	0	0	0.25	0.25	0	0.27
IR15	Gaussian	0.46	0	0	0.12	0.12	-0.01	0.03
IR15_PM	Frank	3.54	0	0	0.18	0.19	0.1	-0.16

A.9. Parameters of the fitted incident wave group energy density - overtopping volume copulas

Table A.4: Summary of semi-correlations and parameters of the fitted wave group energy density - overtopping volume copulas. Note that the subscript E in this table, denotes the empirical semi-correlations which were calculated from the numerical data.

Scenario	Copula	Par1	Par2	λ_U	ρ_N^+	ρ_N^-	$\rho_{N,E}^+$	$\rho_{N,E}^-$
IR11	Gumbel	2.22	0.00	0.63	0.72	0.42	0.77	0.33
IR11_PM	BB8	3.29	0.90	0.00	0.56	0.14	0.54	-0.11
IR11T	Gumbel	2.70	0.00	0.71	0.79	0.53	0.70	0.36
IR11T_PM	Gumbel	2.38	0.00	0.66	0.75	0.46	0.61	0.32
IR15	Gumbel	1.67	0.00	0.48	0.56	0.24	0.37	0.06
IR15_PM	BB7	2.07	0.00	0.60	0.67	0.07	0.59	-0.10

B

Copula functions

Herein, we present the cumulative distribution functions (CDF) of the theoretical copulas which were used in the present study. All definitions follow the work fo (Joe, 2014).

Gaussian

$$C(u,v;\rho) = \Phi_2\left(\Phi^{-1}(u), \Phi^{-1}(v); \rho\right) \tag{B.1}$$

where Φ is the standard normal distribution, Φ_2 is the bivariate standard normal distribution, ρ is the Pearson correlation coefficient and $0 \leq u, v \leq 1$.

Gumbel

$$C(u,v;\delta) = exp\left\{-\left([-logu]^{\delta} + [-logv]^{\delta}\right)^{1/\delta}\right\} \tag{B.2}$$

where $0 \leq u, v \leq 1$ and $1 \leq \delta < \infty$.

BB7

$$C(u,v;\theta,\delta) = 1 - \left(1 - \left[(1-\bar{u}^{\theta})^{-\delta} + (1-\bar{v}^{\theta})^{-\delta} - 1\right]^{-1/\delta}\right)^{1/\theta} \tag{B.3}$$

where: $\bar{u} = 1 - u$, $\bar{v} = 1 - v$, $0 \leq u, v \leq 1$, $\theta \geq 1$ and $\delta > 0$.

BB8

$$C(u,v;\theta,\delta) = \delta^{-1}\left(1 - \{1 - \eta^{-1}[1-(1-\delta u)^{\theta}][1-(1-\delta v)^{\theta}]\}^{1/\theta}\right) \tag{B.4}$$

where $\eta = 1 - (1-\delta)^{\theta}$, $0 \leq u, v \leq 1$, $\theta \leq 1$ and $0 < \delta \leq 1$.

Frank

$$C(u,v;\delta) = -\delta^{-1} log\left(\frac{1 - e^{-\delta} - (1-e^{-\delta u})(1-e^{-\delta v})}{1-e^{-\delta}}\right) \tag{B.5}$$

where $0 \leq u, v \leq 1$.

Bibliography

Adcock, T. A. A., Taylor, P. H., & Draper, S. (2015). Nonlinear dynamics of wave-groups in random seas: Unexpected walls of water in the open ocean. *Proceedings of the Royal Society A: Mathematical, Physical and Engineering Sciences*, *471*(2184), 20150660. https://doi.org/10.1098/rspa.2015.0660

Afshar, M. A. (2010). Numerical wave generation in openfoam®.

Bingham, H. B., & Zhang, H. (2007). On the accuracy of finite-difference solutions for nonlinear water waves. *Journal of Engineering Mathematics*, *58*(1), 211–228.

Brown, S., Greaves, D., Magar, V., & Conley, D. (2016). Evaluation of turbulence closure models under spilling and plunging breakers in the surf zone. *Coastal Engineering*, *114*, 177–193. https://doi.org/https://doi.org/10.1016/j.coastaleng.2016.04.002

Castellino, M., Sammarco, P., Romano, A., Martinelli, L., Ruol, P., Franco, L., & De Girolamo, P. (2018). Large impulsive forces on recurved parapets under non-breaking waves. a numerical study. *Coastal Engineering*, *136*, 1–15. https://doi.org/https://doi.org/10.1016/j.coastaleng.2018.01.012

Chen, W., Warmink, J., van Gent, M., & Hulscher, S. (2021). Numerical modelling of wave overtopping at dikes using openfoam®. *Coastal Engineering*, *166*, 103890. https://doi.org/https://doi.org/10.1016/j.coastaleng.2021.103890

Coles, S. (2001). *An introduction to statistical modeling of extreme values*. Springer.

Corbella, S., & Stretch, D. D. (2013). Simulating a multivariate sea storm using archimedean copulas. *Coastal Engineering*, *76*, 68–78. https://doi.org/https://doi.org/10.1016/j.coastaleng.2013.01.011

De Michele, C., Salvadori, G., Passoni, G., & Vezzoli, R. (2007). A multivariate model of sea storms using copulas. *Coastal Engineering*, *54*(10), 734–751. https://doi.org/https://doi.org/10.1016/j.coastaleng.2007.05.007

Dermentzoglou, D. (2021). Crownwalls with a fully curved face: An experimental study.

Devolder, B., Troch, P., & Rauwoens, P. (2018). Performance of a buoyancy-modified k-ω and k-ω sst turbulence model for simulating wave breaking under regular waves using openfoam®. *Coastal Engineering*, *138*, 49–65. https://doi.org/https://doi.org/10.1016/j.coastaleng.2018.04.011

Dimakopoulos, A., & Higuera, P. (2021). Wave generation and absorption techniques. In *Advanced numerical modelling of wave structure interactions* (pp. 1–35). CRC Press.

Dimakopoulos, A. S., Cuomo, G., & Chandler, I. (2016). Optimized generation and absorption for three-dimensional numerical wave and current facilities. *Journal of Waterway, Port, Coastal, and Ocean Engineering*, *142*(4), 06016001. https://doi.org/10.1061/(ASCE)WW.1943-5460.0000324

Dong, S., Wang, N., Lu, H., & Tang, L. (2015). Bivariate distributions of group height and length for ocean waves using copula methods. *Coastal Engineering*, *96*, 49–61. https://doi.org/https://doi.org/10.1016/j.coastaleng.2014.11.005

Embrechts, P., McNeil, A., & Straumann, D. (2002). Correlation and dependence in risk management: Properties and pitfalls. *Risk management: value at risk and beyond*, *1*, 176–223.

Engsig-Karup, A., Bingham, H., & Lindberg, O. (2009). An efficient flexible-order model for 3d nonlinear water waves. *Journal of Computational Physics*, *228*(6), 2100–2118. https://doi.org/https://doi.org/10.1016/j.jcp.2008.11.028

Franco, L., De Gerloni, M., & Van der Meer, J. (1995). Wave overtopping on vertical and composite breakwaters, 1030–1045.

Funke, E. R., & Mansard, E. P. D. (1979). On the synthesis of realistic sea states in a laboratory flume.

Goda, Y., & Suzuki, Y. (1976). Estimation of incident and reflected waves in random wave experiments. In *Coastal engineering 1976* (pp. 828–845). https://doi.org/10.1061/9780872620834.048

Gunbak, A., & Bruun, P. (1979). Wave mechanics principles on the design of rubble-mound breakwaters. *Proc. Port and Oc. Engrg. Under Artic Conditions POAC*, *79*, 1301–1318.

Haller, M. C., & Dalrymple, R. A. (1995). Looking for wave groups in the surf zone. *Proc. Coastal Dynamics*, *95*, 81–92.

Higuera, P., Lara, J. L., & Losada, I. J. (2013). Simulating coastal engineering processes with openfoam®. *Coastal Engineering*, *71*, 119–134. https://doi.org/https://doi.org/10.1016/j.coastaleng.2012.06.002

Higuera, P., Lara, J. L., & Losada, I. J. (2014). Three-dimensional interaction of waves and porous coastal structures using openfoam®. part ii: Application. *Coastal Engineering*, *83*, 259–270.

Hofland, B., Wenneker, I., & Van Steeg, P. (2014). Short test durations for wave overtopping experiments.

Huang, L., Li, Y., Benites-Munoz, D., Windt, C. W., Feichtner, A., Tavakoli, S., Davidson, J., Paredes, R., Quintuna, T., Ransley, E., Colombo, M., Li, M., Cardiff, P., & Tabor, G. (2022). A review on the modelling of wave-structure interactions based on openfoam. *OpenFOAM® Journal*, *2*, 116–142. https://doi.org/10.51560/ofj.v2.65

Huang, W., & Dong, S. (2021). Statistical description of wave groups in three types of sea states. *Ocean Engineering*, *225*, 108745. https://doi.org/https://doi.org/10.1016/j.oceaneng.2021.108745

Jacobsen, N. G., Fuhrman, D. R., & Fredsøe, J. (2012). A Wave Generation Toolbox for the Open-Source CFD Library: OpenFoam®. *International Journal for Numerical Methods in Fluids*, *70*(9), 1073–1088. https://doi.org/{10.1002/fld.2726}

Jacobsen, N. G., van Gent, M. R., Capel, A., & Borsboom, M. (2018). Numerical prediction of integrated wave loads on crest walls on top of rubble mound structures. *Coastal Engineering*, *142*, 110–124. https://doi.org/https://doi.org/10.1016/j.coastaleng.2018.10.004

Jäger, W. S., & Nápoles, O. M. (2017). A vine-copula model for time series of significant wave heights and mean zero-crossing periods in the north sea. *ASCE-ASME Journal of Risk and Uncertainty in Engineering Systems, Part A: Civil Engineering*, *3*(4), 04017014. https://doi.org/10.1061/AJRUA6.0000917

Jensen, B., Jacobsen, N. G., & Christensen, E. D. (2014). Investigations on the porous media equations and resistance coefficients for coastal structures. *Coastal Engineering*, *84*, 56–72. https://doi.org/https://doi.org/10.1016/j.coastaleng.2013.11.004

Joe, H. (1993). Parametric families of multivariate distributions with given margins. *Journal of Multivariate Analysis*, *46*(2), 262–282. https://doi.org/https://doi.org/10.1006/jmva.1993.1061

Joe, H. (2014). *Dependence modeling with copulas*. CRC press.

Joe, H., & Hu, T. (1996). Multivariate distributions from mixtures of max-infinitely divisible distributions. *Journal of Multivariate Analysis*, *57*(2), 240–265. https://doi.org/https://doi.org/10.1006/jmva.1996.0032

Koosheh, A., Etemad-Shahidi, A., Cartwright, N., Tomlinson, R., & van Gent, M. R. (2021). Individual wave overtopping at coastal structures: A critical review and the existing challenges. *Applied Ocean Research*, *106*, 102476. https://doi.org/https://doi.org/10.1016/j.apor.2020.102476

Laface, V., Malara, G., Kougioumtzoglou, I. A., Romolo, A., & Arena, F. (2018). Nonlinear wave crest distribution on a vertical breakwater. *Coastal Engineering*, *138*, 227–234. https://doi.org/https://doi.org/10.1016/j.coastaleng.2018.04.018

Lanzafame, R., Timmermans, M., Orlin, F., Valls, S. S., & Morales, O. (2021). Probabilistic design for civil engineering infrastructure using vine-copulas.

Larsen, B. E., Fuhrman, D. R., & Roenby, J. (2019). Performance of interfoam on the simulation of progressive waves. *Coastal Engineering Journal*, *61*(3), 380–400. https://doi.org/10.1080/21664250.2019.1609713

Li, F., van Gelder, P., Ranasinghe, R., Callaghan, D., & Jongejan, R. (2014). Probabilistic modelling of extreme storms along the dutch coast. *Coastal Engineering*, *86*, 1–13. https://doi.org/https://doi.org/10.1016/j.coastaleng.2013.12.009

Li, Y., Fredberg, M. B., Larsen, B. E., & Fuhrman, D. R. (2020). Simulating breaking waves with the reynolds stress turbulence model. *Coastal Engineering Proceedings*, (36v), waves.17. https://doi.org/10.9753/icce.v36v.waves.17

Longuet-Higgins, M. S. (1984). Statistical properties of wave groups in a random sea state. *Philosophical Transactions of the Royal Society of London. Series A, Mathematical and Physical Sciences*, *312*(1521), 219–250. https://doi.org/10.1098/rsta.1984.0061

Mares-Nasarre, P., Gómez-Martín, M. E., & Medina, J. R. (2020). Influence of mild bottom slopes on the overtopping flow over mound breakwaters under depth-limited breaking wave conditions. *Journal of Marine Science and Engineering*, *8*(1). https://www.mdpi.com/2077-1312/8/1/3

Martins, K., Blenkinsopp, C. E., Almar, R., & Zang, J. (2017). The influence of swash-based reflection on surf zone hydrodynamics: A wave-by-wave approach. *Coastal Engineering*, *122*, 27–43. https://doi.org/https://doi.org/10.1016/j.coastaleng.2017.01.006

Mayer, S., Garapon, A., & Sørensen, L. S. (1998). A fractional step method for unsteady free-surface flow with applications to non-linear wave dynamics. *International Journal for Numerical Methods in Fluids*, *28*(2), 293–315. https://doi.org/https://doi.org/10.1002/(SICI)1097-0363(19980815)28:2<293::AID-FLD719>3.0.CO;2-1

Missios, K., Jacobsen, N., Moeller, K., & Roenby, J. (2023). Extending the isoadvector geometric vof method to flows in porous media. *OpenFOAM® Journal*, *3*, 66–74. https://doi.org/10.51560/ofj.v3.72

Moeller, K. (2021). Investigating an alternative discretization of the gravitional force when simulating interfacial flows using the interIsoFoam solver. In H. Nilsson (Ed.), *Cfd with opensource software*. https://doi.org/http://dx.doi.org/10.17196/OS_CFD#YEAR_2021

Molines, J., Herrera, M. P., Gómez-Martín, M. E., & Medina, J. R. (2019). Distribution of individual wave overtopping volumes on mound breakwaters. *Coastal Engineering*, *149*, 15–27. https://doi.org/https://doi.org/10.1016/j.coastaleng.2019.03.006

Moretto, M. (2020). An efficient numerical approach to model wave overtopping of rubble mound breakwaters.

Orcel, O., Sergent, P., & Ropert, F. (2021). Trivariate copula to design coastal structures. *Natural Hazards and Earth System Sciences*, *21*(1), 239–260. https://doi.org/10.5194/nhess-21-239-2021

Patil, A. (2019). Numerical investigation of nearshore wave transformation and surf zone hydrodynamics.

Paulsen, B. T., Bredmose, H., & Bingham, H. B. (2014). An efficient domain decomposition strategy for wave loads on surface piercing circular cylinders. *Coastal Engineering*, *86*, 57–76. https://doi.org/https://doi.org/10.1016/j.coastaleng.2014.01.006

Pullen, T., Allsop, N., Bruce, T., Kortenhaus, A., Schüttrumpf, H., & Van der Meer, J. (2007). *Eurotop wave overtopping of sea defences and related structures: Assessment manual*.

Raby, A., Jayaratne, R., Bredmose, H., & Bullock, G. (2020). Individual violent wave-overtopping events: Behaviour and estimation. *Journal of Hydraulic Research*, *58*(1), 34–46. https://doi.org/10.1080/00221686.2018.1555549

Roenby, J., Bredmose, H., & Jasak, H. (2016). A computational method for sharp interface advection. *Royal Society Open Science*, *3*(11), 160405. https://doi.org/10.1098/rsos.160405

Roenby, J., Bredmose, H., & Jasak, H. (2019). Isoadvector: Geometric vof on general meshes. In *Openfoam®* (pp. 281–296). Springer.

Roenby, J., Larsen, B. E., Bredmose, H., & Jasak, H. (2017). A new volume-of-fluid method in openfoam. *MARINE VI: Proceedings of the VI International Conference on Computational Methods in Marine Engineering*, 266–277.

Romano, A., Bellotti, G., Briganti, R., & Franco, L. (2015). Uncertainties in the physical modelling of the wave overtopping over a rubble mound breakwater: The role of the seeding number and of the test duration. *Coastal Engineering*, *103*, 15–21. https://doi.org/https://doi.org/10.1016/j.coastaleng.2015.05.005

Rusche, H. (2002). *Computational fluid dynamics of dispersed two-phase flows at high phase fractions* (Doctoral dissertation).

Rusche, H. (2003). *Computational fluid dynamics of dispersed two-phase flows at high phase fractions* (Doctoral dissertation). Imperial College London (University of London).

Sklar, A. (1959). Fonctions de r´epartition ‘a n dimensions et leurs marges. *Publications de l’Institut de Statistique de L’Universit´e de Paris*, *8*, 229–231.

Sobey, R. J., & Liang, H.-B. (1987). Complex envelope identification of wave groups. In *Coastal engineering 1986* (pp. 752–766).

Spearman, C. (1904). The proof and measurement of association between two things. *The American Journal of Psychology*, *15*, 72–101. https://doi.org/10.2307/1412159

Spearman rank correlation coefficient. (2008). In *The concise encyclopedia of statistics* (pp. 502–505). Springer New York. https://doi.org/10.1007/978-0-387-32833-1_379

Torrence, C., & Compo, G. P. (1998). A practical guide to wavelet analysis. *Bulletin of the American Meteorological Society*, *79*(1), 61–78. https://doi.org/https://doi.org/10.1175/1520-0477(1998)079<0061:APGTWA>2.0.CO;2

Tromans, P. S., Anaturk, A. R., & Hagemeijer, P. (1991). A new model for the kinematics of large ocean waves-application as a design wave. *The first international offshore and polar engineering conference*.

van der Meer, J., Allsop, W., Bruce, T., Rouck, J., Kortenhaus, A., Pullen, T., Schüttrumpf, H., Troch, P., & Zanuttigh, B. (2018). *Eurotop 2018: Manual on wave overtopping of sea defences and related sturctures - an overtopping manual largely based on european research, but for worlwide application (2nd edition)*. http://www.overtopping-manual.com/

van Gorsel, J. (2021). Numerical analysis of broken regular wave forces on a shoal-mounted cylinder.

Weller, H. G., Tabor, G., Jasak, H., & Fureby, C. (1998). A tensorial approach to computational continuum mechanics using object-oriented techniques. *Computers in Physics*, *12*(6), 620–631. https://doi.org/10.1063/1.168744

Whittaker, C., Fitzgerald, C., Raby, A., Taylor, P., & Borthwick, A. (2018). Extreme coastal responses using focused wave groups: Overtopping and horizontal forces exerted on an inclined seawall. *Coastal Engineering*, *140*, 292–305. https://doi.org/https://doi.org/10.1016/j.coastaleng.2018.08.004

Williams, H. E., Briganti, R., & Pullen, T. (2014). The role of offshore boundary conditions in the uncertainty of numerical prediction of wave overtopping using non-linear shallow water equations. *Coastal Engineering*, *89*, 30–44. https://doi.org/https://doi.org/10.1016/j.coastaleng.2014.03.003

Zelt, J., & Skjelbreia, J. E. (1992). Estimating incident and reflected wave fields using an arbitrary number of wave gauges. *Coastal Engineering Proceedings*, *1*(23). https://doi.org/10.9753/icce.v23.\%p

Zhang, Y., Kim, C.-W., Beer, M., Dai, H., & Soares, C. G. (2018). Modeling multivariate ocean data using asymmetric copulas. *Coastal Engineering*, *135*, 91–111. https://doi.org/https://doi.org/10.1016/j.coastaleng.2018.01.008